

Response to review comments on acp-2016-453

The original comments are provided in black, our response is given in red.

The revised manuscript documents the differences in meteorological, chemical and aerosol properties in 1 year WRF-Chem simulations of eastern North America at 12km (WRF12/WRF12-remap) and 60km (WRF60) horizontal resolution and investigates some of the reasons of the different performance between the two resolutions. Among other reasons a dry bias in the specific humidity in the boundary layer and a substantial underestimation of total monthly precipitation in WRF60 are identified as causes for the better performance of WRF12/WRF12-remap over WRF60. This is important for the topic of the study and needs to be mentioned in the abstract. After this minor change the manuscript is recommended for publication.

As indicated by the reviewer we modified the abstract as follows:

“Some of the enhanced model performance for AOD appears to be attributable to improved simulation of meteorological conditions and the concentration of key aerosol precursor gases (e.g. SO₂ and NH₃). Among other reasons, a dry bias in the specific humidity in the boundary layer and a substantial underestimation of total monthly precipitation in the 60 km simulations are identified as causes for the better performance of WRF-Chem simulations at 12 km.”

1 **The impact of resolution on meteorological, chemical and**
2 **aerosol properties in regional simulations with WRF-Chem**

3

4 P. Crippa¹, R. C. Sullivan², A. Thota³, S. C. Pryor^{2,3}

5

6

7 ¹COMET, School of Civil Engineering and Geosciences, Cassie Building, Newcastle
8 University, Newcastle upon Tyne, NE1 7RU, UK

9 ²Department of Earth and Atmospheric Sciences, Bradfield Hall, 306 Tower Road, Cornell
10 University, Ithaca, NY 14853, USA

11 ³Pervasive Technology Institute, Indiana University, Bloomington, IN 47405, USA

12

13 *Correspondence to:* P. Crippa (paola.crippa@ncl.ac.uk), School of Civil Engineering and
14 Geosciences, Cassie Building, Room G15, Telephone: +44 (0)191 208 5041, Newcastle
15 University, Newcastle upon Tyne, NE1 7RU, UK

16 **Abstract**

17 Limited area (regional) models applied at high resolution over specific regions of interest are
18 generally expected to more accurately capture the spatio-temporal variability of key
19 meteorological and climate parameters. However, improved performance is not inevitable, and
20 there remains a need to optimize use of numerical resources, and to quantify the impact on
21 simulation fidelity that derives from increased resolution. The application of regional models
22 for climate forcing assessment is currently limited by the lack of studies quantifying the
23 sensitivity to horizontal spatial resolution and the physical-dynamical-chemical schemes
24 driving the simulations. Here we investigate model skill in simulating meteorological, chemical
25 and aerosol properties as a function of spatial resolution, by applying the Weather Research
26 and Forecasting model with coupled Chemistry (WRF-Chem) over eastern North America at
27 different resolutions. Using Brier Skill Scores and other statistical metrics it is shown that
28 enhanced resolution (from 60 to 12 km) improves model performance for all of the
29 meteorological parameters and gas phase concentrations considered, in addition to both mean
30 and extreme Aerosol Optical Depth (AOD) in three wavelengths in the visible relative to
31 satellite observations, principally via increase of potential skill. Some of the enhanced model
32 performance for AOD appears to be attributable to improved simulation of meteorological
33 conditions (~~notably precipitation and near-surface specific humidity~~) and the concentration of
34 key aerosol precursor gases (e.g. SO₂ and NH₃). Among other reasons, a dry bias in the specific
35 humidity in the boundary layer and a substantial underestimation of total monthly precipitation
36 in the 60 km simulations are identified as causes for the better performance of WRF-Chem
37 simulations at 12 km.

38

39

40 **Keywords:** added value, high-resolution WRF-Chem simulations, precipitation, aerosol
41 optical properties, extreme AOD

42 **1 Motivation and Objectives**

43 Aerosols alter Earth's radiation balance primarily by scattering or absorbing incoming solar
44 radiation (direct effect, dominated by accumulation mode (diameters \sim wavelength (λ), where
45 total extinction is often quantified using AOD), or regulating cloud formation/properties by
46 acting as cloud condensation nuclei (CCN) (indirect effect, dominated by diameters \geq 100 nm,
47 magnitude = $f(\text{composition})$). Most aerosols (excluding black carbon) have a larger scattering
48 cross-section than absorption cross-section, and act as CCN thus enhancing cloud albedo and
49 lifetimes. Hence increased aerosol concentrations are generally (but not uniformly) associated
50 with surface cooling (offsetting a fraction of greenhouse gas warming) (Boucher, 2013; Myhre
51 et al., 2013b) to a degree that is principally dictated by the aerosol concentration, size and
52 composition, in addition to the underlying surface and height of the aerosol layer (McComiskey
53 et al., 2008). Despite major advances in measurement and modeling, both the current global
54 mean aerosol direct effect (possible range: -0.77 to $+0.23 \text{ W m}^{-2}$) and the indirect effect
55 (possible range: -1.33 to -0.06 W m^{-2}) remain uncertain (Stocker, 2013), as does their future
56 role in climate forcing (Rockel et al., 2008) and regional manifestations (Myhre et al., 2013a).
57 Specific to our current study region (eastern N. America), one analysis using the NASA GISS
58 global model found that the "regional radiative forcing from US anthropogenic aerosols elicits
59 a strong regional climate response, cooling the central and eastern US by $0.5\text{--}1.0 \text{ }^\circ\text{C}$ on average
60 during 1970–1990, with the strongest effects on maximum daytime temperatures in summer
61 and autumn. Aerosol cooling reflects comparable contributions from direct and indirect
62 radiative effects" (Leibensperger et al., 2012). A recent comparison of multiple global models
63 conducted under the AEROCOM-project indicated this is also a region that exhibits very large
64 model-to-model variability in simulated AOD ($\langle \text{AOD} \rangle \sim 0.5$, $\sigma(\text{AOD}) \sim 1$) (Myhre et al.,
65 2013a).

66 Major reasons why aerosol radiative forcing on both the global and regional scales remains
67 uncertain include short atmospheric residence times and high spatio-temporal variability of
68 aerosol populations, and the complexity of the processes that dictate aerosol concentrations,
69 composition and size distributions (Seinfeld and Pandis, 2016). Although aerosol processes
70 and properties are increasingly being treated in the global Earth System Models (ESMs) (Long
71 et al., 2015; Tilmes et al., 2015) applied in the Coupled Model Intercomparison Project Phase
72 6 (CMIP-6) (Meehl et al., 2014), the scales on which such models are applied remain much
73 coarser than those on which aerosol population properties are known to vary (Anderson et al.,
74 2003). Therefore, limited area atmospheric models (regional models) applied at higher

75 resolution over specific regions of interest are expected to ‘add value’ (i.e. improve the fidelity)
76 of the physical-dynamical-chemical processes that induce extreme events and dictate climate
77 forcing. There is empirical evidence to suggest a strong resolution dependence in simulated
78 aerosol particle properties. For example, WRF-Chem simulations with spatial resolution
79 enhanced from 75 km to 3 km exhibited higher correlations and lower bias relative to
80 observations of aerosol optical properties over Mexico likely due to more accurate description
81 of emissions, meteorology and of the physicochemical processes that convert trace gases to
82 particles (Gustafson et al., 2011;Qian et al., 2010). This improvement in the simulation of
83 aerosol optical properties implies a reduction of the uncertainty in associated aerosol radiative
84 forcing (Gustafson et al., 2011). Further, WRF-Chem run over the United Kingdom and
85 Northern France at multiple resolutions in the range of 40-160 km, underestimated AOD by
86 10-16% and overestimated CCN by 18-36% relative to a high resolution run at 10 km, partly
87 as a result of scale dependence of the gas-phase chemistry and differences in the aerosol uptake
88 of water (Weigum et al., 2016).

89 However, debate remains regarding how to objectively evaluate model performance, quantify
90 the value added by enhanced resolution (Di Luca et al., 2015;Rockel et al., 2008) and on
91 possible limits to the improvement of climate representation in light of errors in the driving
92 “imperfect lateral boundary conditions” (Diaconescu and Laprise, 2013). Nevertheless,
93 although “it is unrealistic to expect a vast amount of added values since models already
94 performs rather decently” (Di Luca et al., 2015) and global ESMs are now run at much higher
95 resolution than in the past, it is generally assumed that high resolution regional models will add
96 value via more realistic representation of spatio-temporal variability than global coarser-
97 resolution simulations. Further, “the main added value of a regional climate model is provided
98 by its small scales and its skill to simulate extreme events, particularly for precipitation”
99 (Diaconescu and Laprise, 2013).

100 It is particularly challenging to assess the added-value from enhanced resolution in the context
101 of climate-relevant aerosol properties since they are a complex product of the fidelity of the
102 simulation of meteorological parameters, gas-phase precursors, emissions and the treatment of
103 aerosol dynamics. Here we quantify the value added by enhanced resolution in the description
104 of physical and chemical atmospheric conditions using year-long simulations from WRF-Chem
105 over eastern North America, and investigate how they impact AOD. The primary performance
106 evaluation of aerosol properties focuses on AOD at different wavelengths ($\lambda = 470, 550$ and
107 660 nm, where the AOD at different λ is used as a proxy of the aerosol size distribution (Tomasi

108 et al., 1983), see details in Sect. 2.3) and is measured relative to observations from satellite-
109 borne instrumentation. Thus the term “value-added” is used here in the context of columnar
110 aerosol properties to refer to an improvement of model performance in simulation of
111 wavelength specific AOD as measured by the MODerate resolution Imaging
112 Spectroradiometer (MODIS) instrument aboard the polar-orbiting Terra satellite. To attribute
113 sources of the enhanced fidelity of AOD, our analysis also incorporates evaluation of the value-
114 added by enhanced resolution in terms of key meteorological and gas-phase drivers of aerosol
115 concentrations and composition and is conducted relative to the MERRA-2 reanalysis product
116 for the physical variables and columnar gas concentrations from satellite observations (see
117 details of the precise data sets used given below). The meteorological parameters considered
118 are air temperature at 2 m (T_{2m}), total monthly precipitation (PPT), planetary boundary-layer
119 height ($PBLH$) and specific humidity in the boundary layer (Q_{PBL}). The gas phase
120 concentrations considered are sulfur dioxide (SO_2), ammonia (NH_3), nitrogen dioxide (NO_2)
121 and formaldehyde (HCHO).

122 We begin by quantifying the performance of WRF-Chem when applied over eastern North
123 America at a resolution of 60 km (WRF60) (~ finest resolution likely to be employed in CMIP-
124 6 global simulations) and then compare the results to those from simulations conducted at 12
125 km (WRF12) (simulation details are given in Table 1). Quantification of model skill is
126 undertaken by mapping the WRF12 output to the WRF60 grid (WRF12-remap) and computing
127 Brier Skill Scores (BSS) using MODIS as the target, WRF60 as the reference forecast and
128 WRF12-remap as the forecast to be evaluated. We also evaluate the performance of the WRF-
129 Chem simulations of 2008 relative to climatology as represented by MODIS observations for
130 2000-2014. We additionally assess the impact of simulation resolution on extreme AOD values
131 that are associated with enhanced impacts on climate and human health. This analysis uses both
132 *Accuracy* and *Hit Rate* as the performance metrics and focuses on the co-occurrence of extreme
133 values in space from the model output and MODIS.

134 Based on the performance evaluation of the WRF-Chem simulations that indicate substantial
135 dry bias in the WRF60 simulations and large seasonality in the skill-scores for AOD as a
136 function of resolution, we conducted two further year-long simulations at 60 km. In the first
137 we held all other simulation conditions constant but selected a different cumulus
138 parameterization. In the second, we held all simulation conditions constant but employed a
139 different set of lateral boundary conditions for the meteorology. In the context of the
140 precipitation biases reported herein it is worthy of note that discrepancies in simulated

141 precipitation regimes are key challenges in regional modelling (both physical and coupled with
142 chemistry). Although the Grell 3D scheme has been successfully applied in a number of prior
143 analysis wherein the model was applied at resolutions in the range of 1-36 km (e.g. (Grell and
144 Dévényi, 2002;Lowrey and Yang, 2008;Nasrollahi et al., 2012;Sun et al., 2014;Zhang et al.,
145 2016)), the North American Regional Climate Change Assessment Program (NARCCAP)
146 simulations with WRF at 50-km were also dry biased in the study domain (Mearns et al., 2012).
147 Although there have been a number of studies that have sought to evaluate different cumulus
148 schemes over different regions at different resolutions, no definitive recommendation has been
149 made regarding the dependence of model skill on resolution and cumulus parameterization
150 (Arakawa, 2004;Jankov et al., 2005;Nasrollahi et al., 2012;Li et al., 2014). Hence, further
151 research is needed to identify the optimal cumulus scheme for use over North America at
152 coarser resolution. Thus, we performed a sensitivity analysis on the cumulus scheme at 60 km
153 by applying the Grell-Freitas parameterization (Grell and Freitas, 2014), which is the next
154 generation of the Grell 3D scheme.

155 **2 Materials and Methods**

155 **2.1 WRF-Chem simulations**

156 WRF-Chem (version 3.6.1) simulations were performed for the calendar year 2008 over eastern
157 North America, in a domain centered over southern Indiana (86°W, 39°N) at two resolutions,
158 one close to the finest resolution designed for CMIP-6 global model runs (i.e. 60 km, WRF60)
159 and the other one at much higher resolution (12 km, WRF12). Simulation settings are identical
160 for the two runs except for the time-step used for the physics (Table 1). Physical and chemical
161 parameterizations were chosen to match previous work using WRF-Chem at 12 km on the same
162 region which showed good performance relative to observations and the year 2008 was selected
163 because it is representative of average climate and aerosol conditions during 2000 - 2014
164 (Crippa et al., 2016). More specifically the simulations adopted the RADM2 chemical
165 mechanism (Stockwell et al., 1990) and a modal representation of the aerosol size distribution
166 (MADE/SORGAM, (Ackermann et al., 1998;Schell et al., 2001)) with three lognormal modes
167 and fixed geometric standard deviations (i.e. 1.7, 2 and 2.5 for Aitken, accumulation and coarse
168 mode, respectively (Ackermann et al., 1998;Grell et al., 2005)). Aerosol direct feedback was
169 turned on and coupled to the Goddard shortwave scheme (Fast et al., 2006). A telescoping
170 vertical grid with 32 model layers from the surface to 50 hPa and 10 layers up to 800 hPa was
171 selected. Meteorological initial and boundary conditions from the North American Mesoscale
172 Model at 12 km resolution (NAM12) are applied every 6 hours, while initial and chemical
173 boundary conditions are taken from MOZART-4 (Model for Ozone and Related chemical

174 Tracers, version 4) with meteorology from NCEP/NCAR-reanalysis (Emmons et al., 2010).
175 Anthropogenic emissions are specified for both WRF60 and WRF12 from the US National
176 Emission Inventory 2005 (NEI-05) (US-EPA, 2009) which provides hourly point and area
177 emissions at 4 km on 19 vertical levels. The simulation settings and specifically the use of a
178 modal representation of the aerosol size distribution were selected to retain computational
179 tractability. Accordingly, the 60 km simulations for the year 2008 completed in 6.4 hours
180 whereas the 12 km simulations completed in 9.5 days (230 hours) on the Cray XE6/XK7
181 supercomputer (Big Red II) owned by Indiana University, using 256 processors distributed on
182 8 nodes.

183 As described in detail below, in the WRF60 simulations configured as described in Table 1,
184 simulated precipitation during the summer months exhibits substantial dry bias, and the
185 analysis of value added by enhanced simulation resolution exhibited strong seasonality. We
186 performed a sensitivity analysis to the cumulus scheme, by conducting an additional year-long
187 simulation at 60 km using the Grell-Freitas parameterization (Grell and Freitas, 2014), which
188 is an evolution of Grell 3D that is scale-aware and treats some aspects of aerosol-cloud
189 interactions. We also tested the sensitivity of the simulation results to the meteorological
190 boundary conditions, by repeating the WRF60 simulations using output from the Global
191 Forecast System (GFS) at 0.5° resolution every 6 hours to provide the lateral boundary
192 conditions.

193 **2.2 Observations**

194 Model aerosol optical properties are evaluated relative to the MODIS Collection 6 dark-target
195 land aerosol product from aboard the Terra satellite (~1030 overpass local solar time (LST))
196 (Levy et al., 2013). To provide a consistent assessment of model skill, the evaluation of AOD
197 is conducted only on land areas since the MODIS dark-target ocean aerosol product is based
198 on a retrieval algorithm different from the one over land (Levy et al., 2013). Trace gas
199 concentrations are evaluated relative to measurements from the Ozone Monitoring Instrument
200 (OMI; version 3) (Chance, 2002) and the Infrared Atmospheric Sounding Interferometer (IASI;
201 NN version 1) (Whitburn et al., 2016) aboard the Aura (~1345 LST) and MetOp satellites
202 (~0930 LST), respectively. MODIS retrieves AOD at multiple λ including 470, 550, and 660
203 nm, and the MODIS algorithm removes cloud-contaminated pixels prior to spatial averaging
204 over 10×10 km (at nadir). OMI and IASI have nadir resolutions of 13×24 km and 12 km
205 (circular footprint), respectively, and have been filtered to remove retrievals with cloud

206 fractions > 0.3 (Fioletov et al., 2011; McLinden et al., 2014; Vinken et al., 2014) and OMI pixels
207 affected by the row anomalies. MODIS, OMI, and IASI provide near daily global coverage,
208 although the row anomalies render portions of the OMI viewing swath unusable. Uncertainty
209 in AOD from MODIS is spatially and temporally variable. It has been estimated as $\pm (0.05 +$
210 $15\%)$ for AOD over land (Levy et al., 2013), and prior research has reported 71% of MODIS
211 Collection 5 retrievals fall within $0.05 \pm 20\%$ for AOD relative to AERONET in the study
212 domain (Hyer et al., 2011). The accuracy of OMI (“root sum of the square of all errors,
213 including forward model, inverse model, and instrument errors” (Brinkma et al., 2003)) is 1.1
214 DU or 50% for SO_2 , $2 \times 10^{14} \text{ cm}^{-2}/30\%$ for background/polluted NO_2 conditions, and 35% for
215 HCHO. This uncertainty is typically reduced by spatial and temporal averaging, as employed
216 herein (Fioletov et al., 2011; Krotkov et al., 2008). IASI NH_3 retrievals do not use an a priori
217 assumption of emissions, vertical distribution, or lifetime of NH_3 (i.e. no averaging kernel);
218 therefore, NH_3 accuracy is variable (Whitburn et al., 2016), and thus only retrievals with
219 uncertainty lower than the retrieved concentrations are used herein.

220 For the model evaluation, satellite observations for each day are regridded to the WRF-Chem
221 discretization. This is done by averaging all valid retrievals within: 0.1° and 0.35° of the WRF-
222 Chem grid-cell center for the $12 \times 12 \text{ km}$ and $60 \times 60 \text{ km}$ resolutions, respectively for MODIS;
223 $0.125^\circ \times 0.18^\circ$ (along-track/latitudinal \times cross-track/longitudinal) and $0.365^\circ \times 0.42^\circ$ for OMI;
224 0.12° and 0.36° for IASI. To avoid issues from under-sampling, we require at least 10 valid
225 MODIS granules for the $60 \times 60 \text{ km}$ daily average to be computed and at least 5 daily averages
226 to compute a monthly average for each grid cell. Model evaluation of gaseous species is
227 performed on a seasonal basis using standard scores (z-scores), which are computed as the
228 difference between the seasonal mean within a grid cell and the seasonal spatial mean, divided
229 by the seasonal spatial standard deviation. Use of z-scores allows comparison of the spatial
230 patterns of satellite observations and model output in terms of standard deviation units from
231 the mean.

232 The simulated meteorological properties are evaluated using Modern-Era Retrospective
233 analysis for Research and Applications (MERRA-2) reanalysis data as the target. MERRA-2
234 is a homogenized and continuous in time description of atmospheric properties on a 3-
235 dimensional global grid (horizontal resolution of $0.5^\circ \times 0.625^\circ$, L72), developed by NASA and
236 was released in Fall 2015 (Molod et al., 2015). MERRA-2 provides hourly values of T_{2m} and
237 $PBLH$, and vertical profile of 3-dimensional variables every 3 hours on a large number of

238 pressure levels. Here we compute the total specific humidity (Q_{PBL}) of the lowest 8 pressure
 239 levels (i.e. in the boundary-layer approximated as the layer from 1000 to 825 hPa) in MERRA-
 240 2, assuming an average air density in the PBL of 1.1 kg m^{-3} . For the evaluation of simulated
 241 precipitation we use accumulated monthly total values.

242 2.3 Spectral dependence of AOD

243 Three properties dictate the actual aerosol direct radiative forcing: AOD, single scattering
 244 albedo and asymmetry factor, all of which are a function of the wavelength (λ) of incident
 245 radiation. The first property is related to the total columnar mass loading, typically dominates
 246 the variability of direct aerosol effect (Chin et al., 2009) and is the focus of the current research.
 247 The relationship between the aerosol size distribution and spectral dependence of AOD is
 248 described by a power law function:

$$249 \quad \beta(\lambda_1) = \beta(\lambda_2) \times \left(\frac{\lambda_1}{\lambda_2} \right)^{-\alpha} \quad (1)$$

250 where β is the particle extinction coefficient at a specific wavelength λ , and α is the Ångström
 251 exponent (Ångström, 1964) which describes the wavelength dependence of AOD (and is
 252 inversely proportional to the average aerosol diameter):

$$253 \quad \alpha = \frac{\ln \frac{AOD(\lambda_1)}{AOD(\lambda_2)}}{\ln \frac{\lambda_2}{\lambda_1}} \quad (2)$$

254 The aerosol volume distribution usually conforms to a multi-lognormal function with n modes:

$$255 \quad \frac{dV(r)}{d \ln r} = \sum_{i=1}^n \frac{C_i}{\sqrt{2\pi}\sigma_i} \exp \left[\frac{-(\ln r - \ln R_i)^2}{2\sigma_i^2} \right] \quad (3)$$

256 where r is the particle radius and C_i , R_i and σ_i are the particle volume concentration, the
 257 geometric mean radius and the standard deviation in the mode i respectively.

258 We can thus compute AOD for a polydisperse distribution of aerosols with refractive index m
 259 in an atmospheric column of height Z as:

$$260 \quad AOD(\lambda) = \int \frac{3\beta(m, r, \lambda)}{4r} \frac{dV(r)}{d \ln r} d \ln r dZ \quad (4)$$

261 As indicated in (Schuster et al., 2006), “the spectral variability of extinction diminishes for
262 particles larger than the incident wavelength”, thus fine mode particles contribute more to AOD
263 in the visible ($\lambda \sim 0.5 \mu\text{m}$) than at longer wavelengths, whereas coarse mode particles provide a
264 similar AOD both at short and long wavelengths. This is reflected in the Ångström parameter
265 which can be thus used as a proxy for the fine mode fraction or fine mode radius (Schuster et
266 al., 2006).

267 **2.4 Quantification of model performance and added-value**

268 Taylor diagrams summarize three aspects of model performance relative to a reference: the
269 spatial correlation coefficient (i.e. Pearson correlation of the fields, r), the ratio of spatial
270 standard deviations of the two spatial fields ($\sigma_{\text{wrf}}/\sigma_{\text{sat}}$) and the root mean squared difference
271 (RMSD) (Taylor, 2001). Here Taylor diagrams are presented for monthly mean AOD from
272 WRF60, WRF12 and WRF12-remap relative to MODIS at different wavelengths (Fig. 1 d-f).
273 Because AOD is not normally distributed, Spearman’s rank correlation coefficients (ρ) of the
274 mean monthly AOD spatial fields are also computed to reduce the impact of a few outliers and
275 the small sample size during cold months (Table 2). To assess the significance of ρ while
276 accounting for multiple testing, we apply a Bonferroni correction (Simes, 1986) in which for
277 m hypothesis tests, the null hypothesis is rejected if $p \leq \frac{\alpha}{m}$, where p is the p-value and α is the
278 confidence level (0.05 is used here).

279 We further quantify the value added (or lack of thereof) of the high-resolution simulations
280 using the following metrics:

281 **(i) Brier Skill Score**

282 Value added is quantified using Brier Skill Scores (BSS) and is evaluated in two ways: first by
283 evaluating the model performance as a function of simulation resolution and then using
284 climatology as the reference ‘forecast’. In these analyses the hourly output from the 12 km
285 resolution simulation is degraded (averaged) to 60 km (hereafter WRF12-remap) as follows:
286 the 12 km domain is resized excluding 2 grid cells at the border to exactly match the 60 km
287 resolution domain. For example, in the analysis of AOD each coarse grid cell thus includes 5×5
288 12 km resolution cells and its value is the mean of all valid 12 km grid cells inside it if at least
289 half of those cells contain valid AOD (i.e. no cloud cover), otherwise the whole coarse cell is
290 treated as missing. In all comparisons of AOD only cells with simultaneous (i.e. model and
291 MODIS) clear sky conditions are considered. A daily value from WRF-Chem is computed as

292 an instantaneous value for the hour nearest to the satellite overpass time. When the comparison
 293 is done on a monthly basis, a monthly mean value is computed from the daily values obtained
 294 under clear sky conditions, only if there are at least five valid observations in the month.

295 The primary metric used to quantify the added value of WRF12-remap versus WRF60 is the
 296 Brier Skill Score (BSS) (Murphy and Epstein, 1989):

$$297 \quad BSS = \frac{r_{F',P'}^2 - \left(r_{F',P'} - \frac{\sigma_{F'}}{\sigma_{P'}} \right)^2 - \left(\frac{\langle P' \rangle - \langle F' \rangle}{\sigma_{P'}} \right)^2 + \left(\frac{\langle P' \rangle}{\sigma_{P'}} \right)^2}{1 + \left(\frac{\langle P' \rangle}{\sigma_{P'}} \right)^2} \quad (5)$$

298 where F is the “forecast” (i.e. the 12 km simulations mapped to 60 km, WRF12-remap); P is
 299 the “target” (i.e. for AOD this is MODIS at 60 km) and output from WRF60 are used as the
 300 reference forecast; F' the difference between 12 km estimates regridded to 60 km and MODIS;
 301 P' the difference between the 60 km simulation and the ‘target’ (i.e. for the AOD MODIS
 302 observations regridded to 60 km). In the analysis of BSS relative to the long-term (15-year)
 303 climatology of AOD from MODIS, the monthly mean climatological value of AOD is used as
 304 the reference forecast, while WRF60 and WRF12-remap are used as the forecasts, and monthly
 305 mean AOD from MODIS at 60 km is the target.

306 BSS measures by how much a test simulation (WRF12-remap) more closely (or poorly)
 307 reproduces observations (from MODIS, MERRA-2 or other satellite products) relative to a
 308 control (WRF60) run. For example, a $BSS > 0$ indicates WRF12, even when regridded to 60 km,
 309 does add value. The first term in (5) ranges from 0 to 1, is described as the potential skill, and
 310 is the square of the spatial correlation coefficient between forecast and reference anomalies to
 311 MODIS. It is the skill score achievable if both the conditional bias (second term) and overall
 312 bias (third term) were zero, and for most of the variables considered herein (particularly AOD)
 313 it contributes to a positive BSS in most calendar months (and seasons). The second term (the
 314 conditional bias, > 0), is the square of the difference between the anomaly correlation
 315 coefficient and the ratio of standard deviation of the anomalies and is small if for all points F'
 316 is linear to P' . The third term is referred to as the forecast anomaly bias, and is the ratio of the
 317 difference between the mean anomalies of WRF12-remap and the observations relative to
 318 WRF60 and the standard deviation of WRF60 anomaly relative to observed values. The fourth
 319 term is the degree of agreement and appears in both the numerator and denominator. It is

320 computed as the square of the ratio of the mean anomaly between WRF60 and observations
321 and the standard deviation of the anomalies.

322 **(ii) Pooled paired t-test**

323 To identify which areas in space contribute most to the AOD added-value, we compare daily
324 mean AOD fields from WRF-Chem at different resolutions and MODIS. We perform a pooled
325 paired t-test to evaluate the null hypothesis that those differences come from normal
326 distributions with equal means and equal but unknown variances (the test statistic has a
327 Student's t distribution with $df = n + m - 2$, and the sample standard deviation is the pooled
328 standard deviation, where n and m are the two sample sizes). The test is conducted by
329 climatological season (e.g. winter = DJF) since there are fewer than 20 valid AOD observations
330 in most 60 km grid cells for each calendar month (Fig. 2). Given the large number of hypothesis
331 tests performed (i.e. one for each 60 km grid cell), we adjust the p-values using the False
332 Discovery Rate (FDR) approach (Benjamini and Hochberg, 1995). In this approach, p-values
333 from the t-tests are ranked from low to high (p_1, p_2, \dots, p_m), then the test with the highest rank, j ,
334 satisfying:

$$335 \quad p_j \leq \frac{j}{m} \alpha \quad (6)$$

336 is identified. Here all p-values satisfying Eq. 6 with $\alpha=0.1$ are considered significant.

337 **(iii) Accuracy and Hit Rate in identification of AOD extremes**

338 For each month we identify grid cells in which the wavelength specific AOD exceeds the 75th
339 percentile value computed from all grid cells and define that as an extreme. Thus grid cells
340 with extreme AOD are independently determined for MODIS and WRF-Chem at different
341 resolutions. The spatial coherence in identification of extremes in the fields is quantified using
342 two metrics: the *Accuracy* and the *Hit Rate (HR)*. The *Accuracy* indicates the overall spatial
343 coherence and is computed as the number of grid cells co-identified as extreme and non-
344 extreme between WRF-Chem and MODIS relative to the total number of cells with valid data.
345 The *HR* weights only correct identification of extremes in MODIS by WRF-Chem.

346 **3 Results**

347 **3.1 Model performance as a function of spatial resolution**

348 When WRF-Chem is applied at 60 km resolution the degree of association of the resulting
349 spatial fields of mean monthly AOD at the three wavelengths with MODIS varies seasonally.

350 Smallest RMSD and highest Spearman spatial correlations (ρ) with MODIS observations
351 generally occur during months with highest mean AOD (i.e. during summer, Fig. 1 d-f and Fig.
352 3), and reach a maximum in August ($\rho = 0.60$, Table 2). However, while the patterns of relative
353 AOD variability are well captured, the absolute magnitudes and spatial gradients of AOD
354 during the summer are underestimated by WRF60 (Fig. 1 d-f and Fig. 3, Table S1). High spatial
355 correlations ($\rho > 0.40$) are also observed in March, April and November (Table 2), when the
356 ratio of spatial standard deviations is closer to 1 (Fig. 1 d-f, Table S1). Only a weak wavelength
357 dependence is observed in the performance metrics as described on Taylor diagrams. The
358 spatial variability is generally more negatively biased for AOD at 660 nm (Table S1), indicating
359 that WRF60 simulations tend to produce larger diameter aerosols homogeneously distributed
360 over the domain, whereas MODIS observations indicate more spatial variability.

361 The performance of WRF60 simulations relative to MODIS contrasts with analyses of WRF12
362 and WRF12-remap. WRF12 and WRF12-remap indicate highest spatial correlations with
363 MODIS observations throughout the summer months ($\rho = 0.5-0.7$, Table 2), although the bias
364 towards simulation of more coarse aerosols than are observed is consistent across the two
365 simulations and with prior research (see details provided in (Crippa et al., 2016)). However,
366 simulations at 12 km (WRF12) show positive ρ with MODIS for all λ in all calendar months,
367 while mean monthly spatial fields of AOD from WRF60 show low and/or negative correlations
368 with MODIS during May, June, September, October and December, indicating substantial
369 differences in the degree of correspondence with MODIS AOD in the two simulations, and
370 higher fidelity of the enhanced resolution runs (Tables 2 and S1).

371 Monthly mean spatial fields of AOD(λ) as simulated by WRF12 or WRF12-remap exhibit
372 positive Spearman correlation coefficients (ρ) with MODIS observations for all calendar
373 months and range from ~ 0.25 for WRF12-remap (0.20 for WRF12) during winter to ~ 0.70
374 and 0.64, respectively during summer (Table 2). Spearman's ρ are uniformly higher in WRF12-
375 remap than WRF12 indicating a mismatch in space in the high-resolution simulation (i.e. that
376 grid cells with high AOD are slightly displaced in the 12 km simulations possibly due to the
377 presence of sub-grid scale aerosol plumes (Rissman et al., 2013)). Mean monthly fields of AOD
378 (all λ) from both WRF12 and WRF12-remap exhibit lower ρ with MODIS in February-April
379 and November than the 60 km runs (Table 2). These discrepancies appear to be driven by
380 conditions in the south of the domain. For example, differences between WRF60/WRF12-
381 remap vs. MODIS during all seasons are significant according to the paired t-test over Florida

382 and along most of the southern coastlines (Fig. 2). This region of significant differences extends
383 up to $\sim 40^\circ\text{N}$ during summer and fall, reflecting the stronger north-south gradient in AOD from
384 MODIS and WRF12-remap that is not captured by WRF60 (see example for $\lambda = 550 \text{ nm}$, Fig.
385 3). These enhancements in the latitudinal gradients from WRF12-remap are also manifest in
386 the physical variables (particularly specific humidity as discussed further below).

387 The differences in the absolute values of mean monthly AOD deriving from differences in the
388 resolution at which WRF-Chem was applied are of sufficient magnitude (a difference of up to
389 0.2 in regions with a mean AOD value of 0.4), particularly in the summer months (Fig. 4), to
390 raise concerns. However, detailed investigation of the simulations settings and repetition of the
391 60 km simulation resulted in virtually identical results indicating no fault can be found in the
392 analysis. Further, we note that the eastern-half of North America was also identified as a region
393 of high discrepancy in global ESM (Myhre et al., 2013a).

394 To further investigate differences in the simulation output due to spatial discretization we
395 computed Brier Skill Scores (BSS). In this analysis AOD for each λ from WRF12-remap are
396 used as the ‘forecast’, output from WRF60 are used as the reference forecast and MODIS
397 observations at 60 km are used as the target. BSS exceed 0 during all months except for
398 September and October, and largest BSS (> 0.5) for AOD (all λ) is found during most months
399 between December and July (Fig. 5a-c). This indicates that running WRF-Chem at 12 km
400 resolution yields higher skill in simulated AOD relative to WRF60, even when the WRF12
401 output is remapped to 60 km. BSS do not strongly depend on λ , indicating the added value
402 from enhanced resolution similarly affects aerosol particles of different sizes. Inspecting the
403 terms defining the BSS provides information about the origin of the added value (Fig. 5a-c).
404 The positive BSS derives principally from the potential skill (first term in Eq. 5), which
405 demonstrates a reduction in bias and/or more accurate representation of the spatial gradients in
406 WRF12-remap. This term exhibits weak seasonality with values below 0.5 only during August
407 and fall months. The second and third terms are close to zero during most months, although
408 bigger biases are found during August-October. The substantial conditional bias during late
409 summer and early fall is the result of the large ratio of standard deviations (> 1 , i.e. the spatial
410 variability of the anomaly relative to MODIS is larger for WRF12-remap than WRF60, Table
411 S1). It thus contributes to the negative BSS found in September and October, which are also
412 identified as outlier months in WRF12-remap from the Taylor diagram analysis (Fig. 1). Output
413 for these months show modest spatial correlations with AOD from MODIS and higher ratio of
414 standard deviations than in WRF60-MODIS comparisons (Fig. 1, Table S1). Previous work

415 showed that the lower model skill (in WRF12) during September and October may be partially
416 attributable to a dry bias in precipitation from WRF-Chem relative to observations. As a result,
417 simulated AOD and near-surface aerosol nitrate and sulfate concentrations are positively biased
418 over large parts of the domain (Crippa et al., 2016). Although the effects of the boundary
419 conditions appear in some variables (e.g. in Fig. 4 and Figs. S1-S3), the BSS results do not
420 significantly change even when those cells are removed from the analysis.

421 When the BSS is used to assess the skill of each model relative to MODIS AOD climatological
422 mean over the years 2000-2014, WRF12-remap is found to add value relative to the
423 climatology (i.e. BSS >0) during summer months and Nov-Jan whereas BSS for WRF60 is
424 positive from late Fall to early Spring (Fig. 5d). The fact that WRF-Chem does not always
425 outperform the climatology is expected since the model is based on time invariant emissions
426 and skill is assessed relative to a year selected to be representative of the AOD climatology.
427 Mean seasonal AOD from MODIS retrievals over the study region during 2008 lie within ± 0.2
428 standard deviations of the climatology (Crippa et al., 2016). Interestingly, BSS for most months
429 (excluding September) are higher for the WRF60 simulations conducted using lateral boundary
430 conditions from NAM12 than GFS.

431 Model resolution also affects the *Accuracy* and *Hit Rate (HR)* for identification of areas of
432 extreme AOD (AOD > 75th percentile). Highest coherence in the identification of extreme AOD
433 in space identified in WRF12-remap (and WRF12) relative to MODIS is found during May-
434 August (*HR* = 53-77%) vs. WRF60 (*HR* = 17-54%, Table 3). Conversely highest *HR* are found
435 for WRF60 and MODIS during winter and early spring, and indeed exceed those for WRF12
436 and WRF12-remap (Table 3, e.g. Feb: *HR* = 0.78 for WRF60, and 0.67 and 0.68 for WRF12
437 and WRF12-remap, respectively). These differences are consistent with the observation that
438 WRF12-remap overestimates the scales of AOD coherence and AOD magnitude during the
439 cold season along coastlines and over much of the domain in April (Fig. 3).

440 The synthesis of these analyses is thus that the higher resolution simulation increases the
441 overall spatial correlation, decreases overall bias in AOD close to the peak of the solar spectrum
442 relative to MODIS observations and therefore the higher-resolution simulations better
443 represent aerosol direct climate forcing. However, WRF12-remap exhibits little improvement
444 over WRF60 in terms of reproducing the spatial variability of AOD in the visible wavelengths
445 and further that WRF12-remap tends to be more strongly positively biased in terms of mean
446 monthly AOD outside of the summer months (Fig. 2 and Fig. 3). Also the improvement in
447 detection of areas of extreme AOD in the higher resolution simulations (WRF12-remap) is

448 manifest only during the warm season.

449 **3.2 Investigating sources of error in simulated AOD**

450 As documented above, WRF-Chem applied at either 60 or 12 km resolution over eastern North
451 America exhibits some skill in reproducing observed spatial fields of AOD and the occurrence
452 of extreme AOD values. However, marked discrepancies both in space and time are found, and
453 at least some of them show a significant dependence on model resolution. Thus, we
454 investigated a range of physical conditions and gas phase concentrations known to be strongly
455 determinant of aerosol dynamics in terms of the BSS as a function of model resolution and also
456 in terms of the mean monthly spatial patterns.

457 WRF12 even when remapped to 60 km provides more accurate description of key
458 meteorological variables such as specific humidity (Q) within the boundary layer, $PBLH$,
459 surface temperature and precipitation (see Fig. 6, S1, S2 and S3) when compared to MERRA-
460 2, as indicated by the positive BSS during almost all months (Fig. 7a). Good qualitative
461 agreement is observed for the spatial patterns and absolute magnitude of T_{2m} in both WRF60
462 and WRF12-remap relative to MERRA-2 for all seasons (Fig. S1) leading to only modest
463 magnitude of BSS (i.e. value added by the higher resolution simulations (Fig. 7a)). The aerosol
464 size distribution and therefore wavelength specific AOD exhibits a strong sensitivity to Q
465 (Santarpia et al., 2005) due to the presence of hygroscopic components in atmospheric aerosols
466 and thus the role of water uptake in determining aerosol diameter, refractivity and extinction
467 coefficient (Zieger et al., 2013). For example, the hygroscopic growth factor, which indicates
468 the change of aerosol diameter due to water uptake, is ~ 1.4 for pure ammonium sulfate with
469 dry diameter of 532 nm at relative humidity of 80%, thus biases in representation atmospheric
470 humidity may lead to big errors in simulated aerosol size and AOD (Flores et al., 2012). Our
471 previous analyses of the 12 km resolution simulations indicated overestimation of sulfate
472 aerosols (a highly hygroscopic aerosol component, and one which in many chemical forms
473 exhibits strong hysteresis (Martin et al., 2004)) relative to observed near-surface $PM_{2.5}$
474 concentrations during all seasons except for winter (Crippa et al., 2016), leading to the
475 hypothesis that simulated AOD and discrepancies therein may exhibit a strong dependence on
476 Q . Consistent with that postulate, Q_{PBL} from WRF12-remap exhibits a moist bias in cloud-free
477 grid cells mostly during warm months, whereas WRF60 is characterized by a dry bias during
478 all seasons (Fig. 6). Despite the positive bias, WRF12-remap better captures the seasonal
479 spatial patterns of Q_{PBL} in MERRA-2, leading to positive BSS for this variable in all calendar
480 months. Thus, there is added value by higher-resolution simulations in representation of one of

481 the key parameters dictating aerosol particle growth and optical properties. Spatial patterns of
482 differences in Q_{PBL} from WRF60 and WRF12-remap relative to MERRA-2 (Fig. 6) exhibit
483 similarities to differences in AOD (Fig. 4). WRF60 is dry-biased relative to WRF12
484 particularly during the summer (and fall) and underestimates Q_{PBL} relative to MERRA-2 during
485 all seasons over the southern states and over most of continental US during summer and fall.
486 Conversely, WRF12-remap overestimates Q_{PBL} over most of continental US during summer
487 and fall relative to MERRA-2.

488 *PBLH* is a key variable for dictating near-surface aerosol concentrations but is highly sensitive
489 to the physical schemes applied, and biases appear to be domain and resolution dependent.
490 However, this parameter is comparatively difficult to assess because differences in *PBLH* from
491 WRF-Chem and MERRA-2 may also originate from the way they are computed (i.e. from heat
492 diffusivity in MERRA-2 (Jordan et al., 2010) and from turbulent kinetic energy in WRF-Chem
493 (Janjić, 2002; von Engeln and Teixeira, 2013)). Nevertheless, the Mellor-Yamada-Janjich *PBL*
494 scheme combined with the Noah Land Surface Model applied in this work was found to
495 produce lower *PBL* heights (Zhang et al., 2009) than other parameterizations. Thus, the positive
496 bias in simulated AOD and surface $PM_{2.5}$ concentrations (reported previously in (Crippa et al.,
497 2016)) may be linked to the systematic underestimation of *PBLH* simulated by WRF12-remap
498 over continental US relative to MERRA-2 during all seasons (except winter) with greatest bias
499 over regions of complex topography (Fig. S2). A positive bias (of several hundred meters) in
500 terms of *PBLH* for WRF simulations using the MYJ parameterization was previously reported
501 for high-resolution simulations over complex terrain (Rissman et al., 2013), and a positive bias
502 in *PBLH* is also observed in the 60 km simulations presented herein (Fig. S2). This may provide
503 a partial explanation for the large negative bias in AOD in WRF60 during summer (Fig. 3). In
504 general, the BSS indicate improvement in the simulation of *PBLH* in WRF12-remap than in
505 WRF60 (Fig. 7a).

506 Consistent with the dry bias in Q_{PBL} in WRF60, total accumulated precipitation is also
507 underestimated in WRF60, while WRF12-remap captures the absolute magnitudes and the
508 spatial patterns therein (Fig. S3). Analyses of hourly precipitation rates also show higher skill
509 for WRF12-remap than WRF60 in simulating precipitation occurrence (*HR*) relative to
510 MERRA-2 (Table S2). More specifically WRF12-remap correctly predicts between 40% and
511 70 % of precipitation events in MERRA-2 with highest skill during winter months, whereas
512 WRF60 output exhibits lower *HR* (~6% during summer and 30% during winter). This result
513 thus confirms our expectation of a strong sensitivity of model performance to resolution due to

514 the inherent scale dependence in the cumulus scheme. Use of the Grell-Freitas parameterization
515 in the WRF60 simulations did not lead to substantially different magnitude and/or spatial
516 patterns of precipitation compared to WRF60 applied with the Grell 3D scheme, and no
517 improvement in agreement with output from MERRA2. The findings of a negative bias in
518 precipitation amounts in WRF60 simulations without a corresponding overestimation of AOD
519 may appear counter-intuitive since aerosol concentrations (and thus AOD) are dependent on
520 aerosol residence times and analyses of sixteen global models from the AeroCom project
521 indicate wet scavenging is the dominant removal process for most aerosol species in the study
522 area (Hand et al., 2012;Textor et al., 2006). However, the negative precipitation bias in WRF60
523 simulations appears to also be linked to poor representation of surface moisture availability,
524 boundary layer humidity (Fig. 6), and ultimately aerosol water content (and hence AOD).

525 Gas phase concentrations (transformed into z-scores) from WRF12-remap show higher
526 agreement with satellite observations during almost all months, as indicated by the positive
527 BSS (Fig. 7b). However given the limited availability of valid satellite observations (especially
528 during months with low radiation intensity), the BSS are likely only robust for the summer
529 months for all species. Nevertheless, with the exception of NH₃ during June, BSS for all months
530 are above or close to zero indicating that on average, the enhanced resolution simulations do
531 exhibit higher skill in the simulation of the gas phase species even when remapped to 60 km
532 resolution. Further, the seasonal average spatial patterns of the total columnar concentrations,
533 expressed in terms of z-scores, also exhibit qualitative agreement with the satellite observations
534 (Fig. S4-S7).

535 **4 Concluding remarks**

536 This analysis is one of the first to quantify the impact of model spatial resolution on the spatio-
537 temporal variability and magnitude of meteorological and chemical parameters and how
538 representation of these variables impact AOD, and does so using simulations for a full calendar
539 year. Application of WRF-Chem at two different resolutions (60 km and 12 km) over eastern
540 North America for a representative year (2008) leads to the following conclusions:

- 541 - Higher-resolution simulations improve the representation of key meteorological
542 variables such as temperature, near-surface specific humidity, boundary layer height
543 and the occurrence and amount of precipitation. Both spatial patterns and precipitation
544 occurrence are better captured by WRF12-remap, and particularly during the summer
545 months the specific humidity within the boundary-layer exhibits closer agreement with

- 546 a reanalysis product when WRF is applied at higher resolution. The dry bias in the low-
547 resolution WRF-Chem simulations (60 km) is consistent with previous research over
548 eastern North America, and is manifest in simulations with two different cumulus
549 parameterizations and two different data sets for the LBC (GFS and NAM12).
- 550 - More accurate representation of spatial patterns and concentration of gaseous species
551 that either play a key role in particle formation and growth or are indicators of primary
552 aerosol emissions is also achieved by running WRF-Chem at high resolution.
 - 553 - Partly/largely due to the improved fidelity of key meteorological parameters and gas-
554 phase aerosol precursor species, higher resolution simulations enhance the fidelity of
555 AOD representation at and near to the peak in the solar spectrum relative to a coarser
556 run. At least some of the improvement in the accuracy with which AOD is reproduced
557 in the higher resolution simulations may be due to improved fidelity of specific
558 humidity and thus more accurate representation of hygroscopic growth of some aerosol
559 components. Spatial correlations of AOD from WRF12 and WRF12-remap with
560 observations from MODIS are higher than AOD from a simulation conducted at 60 km
561 during most months. WRF12 show positive spatial correlations with MODIS for all λ
562 in all calendar months, and particularly during summer ($\rho = 0.5-0.7$). However, the
563 improvement in model performance is not uniform in space and time.
 - 564 - Output from WRF12 and WRF12-remap exhibit highest accord with MODIS
565 observations in capturing the frequency, magnitude and location of extreme AOD
566 values during summer when AOD is typically highest. During May-August WRF12-
567 remap has *Hit Rates* for identification of extreme AOD of 53-78%.

568 It is worthy of note that even the 12 km resolution WRF-Chem simulations exhibit substantial
569 differences in AOD relative to MODIS over eastern North America, and the agreement varies
570 only slightly with wavelength. This may be partially attributable to use of the modal approach
571 to represent the aerosol size distribution in order to enhance computational tractability. In this
572 application each mode has a fixed geometric standard deviation (σ_g), which can lead to biases
573 in simulated AOD in the visible wavelengths by up to 25% (Brock et al., 2016) (with the model
574 overestimating observations if the prescribed σ_g is larger than the observed one). Setting $\sigma_g =$
575 2 for the accumulation mode (the default in WRF-Chem) may lead to an overestimation of the
576 number of particles at the end of the accumulation mode tail, and there is evidence that a value
577 of $\sigma_{g,acc}=1.40$ leads to higher agreement with observations (Mann et al., 2012). Further possible
578 sources of the AOD biases reported herein derive from selection of the physical schemes (e.g.

579 planetary boundary layer (*PBL*) schemes and land-surface model (Misenis and Zhang,
580 2010;Zhang et al., 2009)). Further, it is worth mentioning that NEI emissions are specified
581 based on an average summertime weekday, so enhanced model performance might be achieved
582 if seasonally varying emissions were available.

583 Naturally, there is a need for more research regarding the sensitivity of WRF-Chem simulations
584 of climate relevant aerosol properties to the parameterizations used, the lateral boundary
585 conditions employed and the resolution at which the simulations are conducted. Further,
586 attribution of added-value in the simulation of AOD by enhanced spatial resolution is necessary
587 and will be facilitated by identifying simulation settings that minimize bias in the variables
588 affecting AOD. This research will be part of future investigations.

589 **Acknowledgments**

590 This research was supported in part by a L'Oréal-UNESCO UK and Ireland Fellowship For
591 Women In Science (to PC), the Natural Environmental Research Council (NERC) through the
592 LICS project (ref. NE/K010794/1), grants to SCP from US NSF (grant # 1517365) and NASA
593 (NNX16AG31G), and a NASA Earth and Space Science Fellowship Program - Grant "14-
594 EARTH14F-0207" (to RCS). Further support was provided by the Lilly Endowment, Inc.,
595 through its support for the Indiana University Pervasive Technology Institute and the Indiana
596 METACyt Initiative. We gratefully acknowledge the NASA scientists responsible for
597 MERRA-2 and MODIS products, the developers of WRF-Chem, and Lieven Clarisse, Simon
598 Whitburn, and Martin Van Damme for producing and sharing the NH₃ retrievals. The clarity
599 and content of this manuscript was substantially improved by the comments of three reviewers.

600 **References**

601 Ackermann, I. J., Hass, H., Memmesheimer, M., Ebel, A., Binkowski, F. S., and Shankar, U.:
602 Modal aerosol dynamics model for Europe: development and first applications, *Atmospheric*
603 *Environment*, 32, 2981-2999, [http://dx.doi.org/10.1016/S1352-2310\(98\)00006-5](http://dx.doi.org/10.1016/S1352-2310(98)00006-5), 1998.

604 Anderson, T. L., Charlson, R. J., Winker, D. M., Ogren, J. A., and Holmén, K.: Mesoscale
605 Variations of Tropospheric Aerosols, *Journal of the Atmospheric Sciences*, 60, 119-136, doi:
606 [http://dx.doi.org/10.1175/1520-0469\(2003\)060<0119:MVOTA>2.0.CO;2](http://dx.doi.org/10.1175/1520-0469(2003)060<0119:MVOTA>2.0.CO;2), 2003.

607 Ångström, A.: The parameters of atmospheric turbidity, *Tellus*, 16, 64-75, 10.1111/j.2153-
608 3490.1964.tb00144.x, 1964.

609 Arakawa, A.: The Cumulus Parameterization Problem: Past, Present, and Future, *Journal of*
610 *Climate*, 17, 2493-2525, doi:10.1175/1520-0442(2004)017<2493:RATCPP>2.0.CO;2, 2004.

- 611 Benamini, Y., and Hochberg, Y.: Controlling the False Discovery Rate: A Practical and
612 Powerful Approach to Multiple Testing, *Journal of the Royal Statistical Society. Series B*
613 (Methodological), 57, 289-300, 1995.
- 614 Boucher, O., D. Randall, P. Artaxo, C. Bretherton, G. Feingold, P. Forster, V.-M. Kerminen,
615 Y. Kondo, H. Liao, U. Lohmann, P. Rasch, S.K. Satheesh, S. Sherwood, B. Stevens and X.Y.
616 Zhang: Clouds and Aerosols, in: *Climate Change 2013: The Physical Science Basis.*
617 Contribution of Working Group I to the Fifth Assessment Report of the Intergovernmental
618 Panel on Climate Change, edited by: Stocker, T. F., D. Qin, G.-K. Plattner, M. Tignor, S.K.
619 Allen, J. Boschung, A. Nauels, Y. Xia, V. Bex and P.M. Midgley, Cambridge University Press,
620 Cambridge, United Kingdom and New York, NY, USA, 33–115, 2013.
- 621 Brinksma, E. J., Boersma, K. F., Levelt, P. F., and McPeters, R. D.: OMI validation
622 requirements document, Version 1, Rep. RS-OMIE-KNMI-345, 66, 2003.
- 623 Brock, C. A., Wagner, N. L., Anderson, B. E., Attwood, A. R., Beyersdorf, A., Campuzano-
624 Jost, P., Carlton, A. G., Day, D. A., Diskin, G. S., Gordon, T. D., Jimenez, J. L., Lack, D. A.,
625 Liao, J., Markovic, M. Z., Middlebrook, A. M., Ng, N. L., Perring, A. E., Richardson, M. S.,
626 Schwarz, J. P., Washenfelder, R. A., Welti, A., Xu, L., Ziemba, L. D., and Murphy, D. M.:
627 Aerosol optical properties in the southeastern United States in summer – Part 1: Hygroscopic
628 growth, *Atmospheric Chemistry and Physics*, 16, 25695-25738, doi:10.5194/acp-16-5009-
629 2016, 2016.
- 630 Chance, K.: OMI algorithm theoretical basis document, volume IV: OMI trace gas algorithms,
631 2002.
- 632 Chen, F., and Dudhia, J.: Coupling an advanced land surface–hydrology model with the Penn
633 State–NCAR MM5 modeling system. Part I: model implementation and sensitivity, *Monthly*
634 *Weather Review*, 129, 569-585, doi:10.1175/1520-
635 0493(2001)129<0569:CAALSH>2.0.CO;2, 2001.
- 636 Chin, M., Kahn, R. A., and Schwartz, S. E.: Atmospheric Aerosols Properties and Climate
637 Impacts. A Report by the U.S. Climate Change Science Program and the Subcommittee on
638 Global Change Research, in, National Aeronautics and Space Administration, Washington,
639 D.C., USA, 128, 2009.
- 640 Crippa, P., Sullivan, R. C., Thota, A., and Pryor, S. C.: Evaluating the skill of high-resolution
641 WRF-Chem simulations in describing drivers of aerosol direct climate forcing on the regional
642 scale, *Atmospheric Chemistry and Physics*, 16, 397-416, 10.5194/acp-16-397-2016, 2016.
- 643 Di Luca, A., de Elía, R., and Laprise, R.: Challenges in the Quest for Added Value of Regional
644 Climate Dynamical Downscaling, *Curr Clim Change Rep*, 1, 10-21, 10.1007/s40641-015-
645 0003-9, 2015.
- 646 Diaconescu, E., and Laprise, R.: Can added value be expected in RCM-simulated large scales?,
647 *Climate Dynamics*, 41, 1769-1800, 10.1007/s00382-012-1649-9, 2013.
- 648 Emmons, L. K., Walters, S., Hess, P. G., Lamarque, J. F., Pfister, G. G., Fillmore, D., Granier,
649 C., Guenther, A., Kinnison, D., Laepple, T., Orlando, J., Tie, X., Tyndall, G., Wiedinmyer, C.,
650 Baughcum, S. L., and Kloster, S.: Description and evaluation of the Model for Ozone and

651 Related chemical Tracers, version 4 (MOZART-4), *Geoscientific Model Development*, 3, 43-
652 67, doi:10.5194/gmd-3-43-2010, 2010.

653 Fast, J. D., Gustafson, W. I., Easter, R. C., Zaveri, R. A., Barnard, J. C., Chapman, E. G., Grell,
654 G. A., and Peckham, S. E.: Evolution of ozone, particulates, and aerosol direct radiative forcing
655 in the vicinity of Houston using a fully coupled meteorology-chemistry-aerosol model, *Journal*
656 *of Geophysical Research: Atmospheres*, 111, D21305, 10.1029/2005JD006721, 2006.

657 Fioletov, V. E., McLinden, C. A., Krotkov, N., Moran, M. D., and Yang, K.: Estimation of SO₂
658 emissions using OMI retrievals, *Geophysical Research Letters*, 38, L21811,
659 10.1029/2011GL049402, 2011.

660 Flores, J. M., Bar-Or, R. Z., Bluvshstein, N., Abo-Riziq, A., Kostinski, A., Borrmann, S., Koren,
661 I., Koren, I., and Rudich, Y.: Absorbing aerosols at high relative humidity: linking hygroscopic
662 growth to optical properties, *Atmospheric Chemistry and Physics*, 12, 5511-5521,
663 10.5194/acp-12-5511-2012, 2012.

664 Grell, G. A., and Dévényi, D.: A generalized approach to parameterizing convection combining
665 ensemble and data assimilation techniques, *Geophysical Research Letters*, 29, 38-31-38-34,
666 10.1029/2002GL015311, 2002.

667 Grell, G. A., Peckham, S. E., Schmitz, R., McKeen, S. A., Frost, G., Skamarock, W. C., and
668 Eder, B.: Fully coupled "online" chemistry within the WRF model, *Atmospheric Environment*,
669 39, 6957-6975, 10.1016/j.atmosenv.2005.04.027, 2005.

670 Grell, G. A., and Freitas, S. R.: A scale and aerosol aware stochastic convective
671 parameterization for weather and air quality modeling, *Atmospheric Chemistry and Physics*,
672 14, 5233-5250, 10.5194/acp-14-5233-2014, 2014.

673 Guenther, A., Zimmerman, P., and Wildermuth, M.: Natural volatile organic compound
674 emission rate estimates for U.S. woodland landscapes, *Atmospheric Environment*, 28, 1197-
675 1210, 10.1016/1352-2310(94)90297-6, 1994.

676 Guenther, A. B., Zimmerman, P. R., Harley, P. C., Monson, R. K., and Fall, R.: Isoprene and
677 monoterpene emission rate variability: model evaluations and sensitivity analyses, *J. Geophys.*
678 *Res.-Atmos.*, 98, 12609-12617, 10.1029/93jd00527, 1993.

679 Gustafson, W. I., Qian, Y., and Fast, J. D.: Downscaling aerosols and the impact of neglected
680 subgrid processes on direct aerosol radiative forcing for a representative global climate model
681 grid spacing, *Journal of Geophysical Research: Atmospheres*, 116, D13303,
682 10.1029/2010JD015480, 2011.

683 Hand, J. L., Schichtel, B. A., Pitchford, M., Malm, W. C., and Frank, N. H.: Seasonal
684 composition of remote and urban fine particulate matter in the United States, *J. Geophys. Res.-*
685 *Atmos.*, 117, 10.1029/2011jd017122, 2012.

686 Hong, S.-Y., Dudhia, J., and Chen, S.-H.: A Revised Approach to Ice Microphysical Processes
687 for the Bulk Parameterization of Clouds and Precipitation, *Monthly Weather Review*, 132, 103-
688 120, doi:10.1175/1520-0493(2004)132<0103:ARATIM>2.0.CO;2, 2004.

689 Hyer, E. J., Reid, J. S., and Zhang, J.: An over-land aerosol optical depth data set for data
690 assimilation by filtering, correction, and aggregation of MODIS Collection 5 optical depth
691 retrievals, *Atmospheric Measurement Techniques*, 4, 379-408, 10.5194/amt-4-379-2011,
692 2011.

693 Janjić, Z. I.: The Step-Mountain Eta Coordinate Model: Further Developments of the
694 Convection, Viscous Sublayer, and Turbulence Closure Schemes, *Monthly Weather Review*,
695 122, 927-945, doi:10.1175/1520-0493(1994)122<0927:TSMECM>2.0.CO;2, 1994.

696 Janjić, Z. I.: Nonsingular implementation of the Mellor–Yamada level 2.5 scheme in the NCEP
697 Meso model, NCEP office note, 437, 61, 2002.

698 Jankov, I., A. Gallus, J. W., Segal, M., Shaw, B., and E. Koch, S.: The Impact of Different
699 WRF Model Physical Parameterizations and Their Interactions on Warm Season MCS
700 Rainfall, *Weather and Forecasting*, 20, 1048-1060, doi:10.1175/WAF888.1, 2005.

701 Jordan, N. S., Hoff, R. M., and Bacmeister, J. T.: Validation of Goddard Earth Observing
702 System-version 5 MERRA planetary boundary layer heights using CALIPSO, *J. Geophys.*
703 *Res.-Atmos.*, 115, 10.1029/2009jd013777, 2010.

704 Krotkov, N. A., McClure, B., Dickerson, R. R., Carn, S. A., Li, C., Bhartia, P. K., Yang, K.,
705 Krueger, A. J., Li, Z., Levelt, P. F., Chen, H., Wang, P., and Lu, D.: Validation of SO₂ retrievals
706 from the Ozone Monitoring Instrument over NE China, *Journal of Geophysical Research:*
707 *Atmospheres*, 113, D16S40, 10.1029/2007JD008818, 2008.

708 Leibensperger, E., Mickley, L. J., Jacob, D. J., Chen, W.-T., Seinfeld, J., Nenes, A., Adams,
709 P., Streets, D., Kumar, N., and Rind, D.: Climatic effects of 1950–2050 changes in US
710 anthropogenic aerosols–Part 1: Aerosol trends and radiative forcing, *Atmospheric Chemistry*
711 *and Physics*, 12, 3333-3348, doi:10.5194/acp-12-3333-2012, 2012.

712 Levy, R. C., Mattoo, S., Munchak, L. A., Remer, L. A., Sayer, A. M., Patadia, F., and Hsu, N.
713 C.: The Collection 6 MODIS aerosol products over land and ocean, *Atmospheric Measurement*
714 *Techniques*, 6, 2989-3034, 10.5194/amt-6-2989-2013, 2013.

715 Li, L. F., Li, W. H., and Jin, J. M.: Improvements in WRF simulation skills of southeastern
716 United States summer rainfall: physical parameterization and horizontal resolution, *Climate*
717 *Dynamics*, 43, 2077-2091, 10.1007/s00382-013-2031-2, 2014.

718 Long, M., Yantosca, R., Nielsen, J., Keller, C., da Silva, A., Sulprizio, M., Pawson, S., and
719 Jacob, D.: Development of a grid-independent GEOS-Chem chemical transport model (v9-02)
720 as an atmospheric chemistry module for Earth system models, *Geoscientific Model*
721 *Development*, 8, 595-602, doi:10.5194/gmd-8-595-2015, 2015.

722 Lowrey, M. R. K., and Yang, Z. L.: Assessing the Capability of a Regional-Scale Weather
723 Model to Simulate Extreme Precipitation Patterns and Flooding in Central Texas, *Weather and*
724 *Forecasting*, 23, 1102-1126, 10.1175/2008waf2006082.1, 2008.

725 Mann, G. W., Carslaw, K. S., Ridley, D. A., Spracklen, D. V., Pringle, K. J., Merikanto, J.,
726 Korhonen, H., Schwarz, J. P., Lee, L. A., Manktelow, P. T., Woodhouse, M. T., Schmidt, A.,
727 Breider, T. J., Emmerson, K. M., Reddington, C. L., Chipperfield, M. P., and Pickering, S. J.:
728 Intercomparison of modal and sectional aerosol microphysics representations within the same

729 3-D global chemical transport model, *Atmospheric Chemistry and Physics*, 12, 4449-4476,
730 10.5194/acp-12-4449-2012, 2012.

731 Martin, S. T., Hung, H. M., Park, R. J., Jacob, D. J., Spurr, R. J. D., Chance, K. V., and Chin,
732 M.: Effects of the physical state of tropospheric ammonium-sulfate-nitrate particles on global
733 aerosol direct radiative forcing, *Atmospheric Chemistry and Physics*, 4, 183-214,
734 doi:10.5194/acp-4-183-2004, 2004.

735 McComiskey, A., Schwartz, S. E., Schmid, B., Guan, H., Lewis, E. R., Ricchiazzi, P., and
736 Ogren, J. A.: Direct aerosol forcing: Calculation from observables and sensitivities to inputs,
737 *Journal of Geophysical Research: Atmospheres*, 113, D09202, 10.1029/2007JD009170, 2008.

738 McLinden, C. A., Fioletov, V., Boersma, K. F., Kharol, S. K., Krotkov, N., Lamsal, L., Makar,
739 P. A., Martin, R. V., Veeffkind, J. P., and Yang, K.: Improved satellite retrievals of NO₂ and
740 SO₂ over the Canadian oil sands and comparisons with surface measurements, *Atmospheric
741 Chemistry and Physics*, 14, 3637-3656, 10.5194/acp-14-3637-2014, 2014.

742 Mearns, L. O., Arritt, R., Biner, S., Bukovsky, M., Stain, S., and NARCCAP team The North
743 American Regional Climate Change Assessment Program: Overview of Phase I Results,
744 *Bulletin of the American Meteorological Society*, 93, 1337-1362, 2012.

745 Meehl, G. A., Moss, R., Taylor, K. A., Eyring, V., Stouffer, R. J., Sandrine, B., and Stevens,
746 B.: Climate model intercomparisons: preparing for the next phase, *Eos, Transaction, American
747 Geophysical Union*, 95, 77-84, doi:10.1002/2014EO09, 2014.

748 Misenis, C., and Zhang, Y.: An examination of sensitivity of WRF/Chem predictions to
749 physical parameterizations, horizontal grid spacing, and nesting options, *Atmospheric
750 Research*, 97, 315-334, 10.1016/j.atmosres.2010.04.005, 2010.

751 Mlawer, E. J., Taubman, S. J., Brown, P. D., Iacono, M. J., and Clough, S. A.: Radiative transfer
752 for inhomogeneous atmospheres: RRTM, a validated correlated-k model for the longwave,
753 *Journal of Geophysical Research: Atmospheres*, 102, 16663-16682, 10.1029/97JD00237,
754 1997.

755 Molod, A., Takacs, L., Suarez, M., and Bacmeister, J.: Development of the GEOS-5
756 atmospheric general circulation model: evolution from MERRA to MERRA2, *Geoscientific
757 Model Development*, 8, 1339-1356, 10.5194/gmd-8-1339-2015, 2015.

758 Murphy, A. H., and Epstein, E. S.: Skill scores and correlation-coefficients in model
759 verification, *Monthly Weather Review*, 117, 572-581, 10.1175/1520-
760 0493(1989)117<0572:ssacci>2.0.co;2, 1989.

761 Myhre, G., Samset, B. H., Schulz, M., Balkanski, Y., Bauer, S., Bernsten, T. K., Bian, H.,
762 Bellouin, N., Chin, M., Diehl, T., Easter, R. C., Feichter, J., Ghan, S. J., Hauglustaine, D.,
763 Iversen, T., Kinne, S., Kirkevag, A., Lamarque, J. F., Lin, G., Liu, X., Lund, M. T., Luo, G.,
764 Ma, X., van Noije, T., Penner, J. E., Rasch, P. J., Ruiz, A., Seland, O., Skeie, R. B., Stier, P.,
765 Takemura, T., Tsigaridis, K., Wang, P., Wang, Z., Xu, L., Yu, H., Yu, F., Yoon, J. H., Zhang,
766 K., Zhang, H., and Zhou, C.: Radiative forcing of the direct aerosol effect from AeroCom Phase
767 II simulations, *Atmospheric Chemistry and Physics*, 13, 1853-1877, 10.5194/acp-13-1853-
768 2013, 2013a.

769 Myhre, G., Shindell, D., Bréon, F.-M., Collins, W., Fuglestedt, J., Huang, J., Koch, D.,
770 Lamarque, J.-F., Lee, D., Mendoza, B., Nakajima, T., Robock, A., Stephens, G., Takemura, T.,
771 and Zhang, H.: Anthropogenic and Natural Radiative Forcing, in: *Climate Change 2013: The*
772 *Physical Science Basis. Contribution of Working Group I to the Fifth Assessment Report of*
773 *the Intergovernmental Panel on Climate Change*, edited by: Stocker, T. F., Qin, D., Plattner,
774 G.-K., Tignor, M., Allen, S. K., Boschung, J., Nauels, A., Xia, Y., Bex, V., and Midgley, P.
775 M., Cambridge University Press, Cambridge, United Kingdom and New York, NY, USA, 659–
776 740, 2013b.

777 Nasrollahi, N., AghaKouchak, A., Li, J. L., Gao, X. G., Hsu, K. L., and Sorooshian, S.:
778 Assessing the Impacts of Different WRF Precipitation Physics in Hurricane Simulations,
779 *Weather and Forecasting*, 27, 1003-1016, 10.1175/waf-d-10-05000.1, 2012.

780 Qian, Y., Gustafson Jr, W. I., and Fast, J. D.: An investigation of the sub-grid variability of
781 trace gases and aerosols for global climate modeling, *Atmospheric Chemistry and Physics*, 10,
782 6917-6946, 10.5194/acp-10-6917-2010, 2010.

783 Rissman, J., Arunachalam, S., Woody, M., West, J. J., BenDor, T., and Binkowski, F. S.: A
784 plume-in-grid approach to characterize air quality impacts of aircraft emissions at the
785 Hartsfield–Jackson Atlanta International Airport, *Atmospheric Chemistry and Physics*, 13,
786 9285-9302, 10.5194/acp-13-9285-2013, 2013.

787 Rockel, B., Castro, C. L., Pielke, R. A., von Storch, H., and Leoncini, G.: Dynamical
788 downscaling: Assessment of model system dependent retained and added variability for two
789 different regional climate models, *Journal of Geophysical Research: Atmospheres*, 113,
790 D21107, 10.1029/2007JD009461, 2008.

791 Santarpia, J. L., Gasparini, R., Li, R. J., and Collins, D. R.: Diurnal variations in the
792 hygroscopic growth cycles of ambient aerosol populations, *J. Geophys. Res.-Atmos.*, 110,
793 10.1029/2004jd005279, 2005.

794 Schell, B., Ackermann, I. J., Hass, H., Binkowski, F. S., and Ebel, A.: Modeling the formation
795 of secondary organic aerosol within a comprehensive air quality model system, *J. Geophys.*
796 *Res.-Atmos.*, 106, 28275-28293, 10.1029/2001jd000384, 2001.

797 Schuster, G. L., Dubovik, O., and Holben, B. N.: Angstrom exponent and bimodal aerosol size
798 distributions, *J. Geophys. Res.-Atmos.*, 111, D07207, doi:10.1029/2005JD006328., 2006.

799 Seinfeld, J. H., and Pandis, S. N.: *Atmospheric chemistry and physics: from air pollution to*
800 *climate change*, John Wiley & Sons, 1152 pp., 2016.

801 Simes, R. J.: An improved Bonferroni procedure for multiple tests of significance, *Biometrika*,
802 73, 751-754, 10.2307/2336545, 1986.

803 Simpson, D., Guenther, A., Hewitt, C. N., and Steinbrecher, R.: Biogenic emissions in Europe.
804 1. estimates and uncertainties, *J. Geophys. Res.-Atmos.*, 100, 22875-22890,
805 10.1029/95jd02368, 1995.

806 Stocker, T. F. a. Q., D. and Plattner, G.-K. and Alexander, L.V. and Allen, S.K. and Bindoff,
807 N.L. and Bréon, F.-M. and Church, J.A. and Cubasch, U. and Emori, S. and Forster, P. and
808 Friedlingstein, P. and Gillett, N. and Gregory, J.M. and Hartmann, D.L. and Jansen, E. and

809 Kirtman, B. and Knutti, R. and Krishna Kumar, K. and Lemke, P. and Marotzke, J. and
810 Masson-Delmotte, V. and Meehl, G.A. and Mokhov, I.I. and Piao, S. and Ramaswamy, V. and
811 Randall, D. and Rhein, M. and Rojas, M. and Sabine, C. and Shindell, D. and Talley, L.D. and
812 Vaughan, D.G. and Xie, S.-P.: Summary for Policymakers, in: *Climate Change 2013: The*
813 *Physical Science Basis. Contribution of Working Group I to the Fifth Assessment Report of*
814 *the Intergovernmental Panel on Climate Change*, Cambridge University Press, Cambridge,
815 United Kingdom and New York, NY, USA, 33–115, 2013.

816 Stockwell, W. R., Middleton, P., Chang, J. S., and Tang, X.: The second generation regional
817 acid deposition model chemical mechanism for regional air quality modeling, *Journal of*
818 *Geophysical Research: Atmospheres*, 95, 16343-16367, 10.1029/JD095iD10p16343, 1990.

819 Sun, Y., Yi, L., Zhong, Z., and Ha, Y.: Performance of a New Convective Parameterization
820 Scheme on Model Convergence in Simulations of a Tropical Cyclone at Grey-Zone
821 Resolutions, *Journal of the Atmospheric Sciences*, 71, 2078-2088, doi:10.1175/JAS-D-13-
822 0285.1, 2014.

823 Taylor, K. E.: Summarizing multiple aspects of model performance in a single diagram, *J.*
824 *Geophys. Res.-Atmos.*, 106, 7183-7192, 10.1029/2000jd900719, 2001.

825 Textor, C., Schulz, M., Guibert, S., Kinne, S., Balkanski, Y., Bauer, S., Berntsen, T., Berglen,
826 T., Boucher, O., Chin, M., Dentener, F., Diehl, T., Easter, R., Feichter, H., Fillmore, D., Ghan,
827 S., Ginoux, P., Gong, S., Kristjansson, J. E., Krol, M., Lauer, A., Lamarque, J. F., Liu, X.,
828 Montanaro, V., Myhre, G., Penner, J., Pitari, G., Reddy, S., Seland, O., Stier, P., Takemura, T.,
829 and Tie, X.: Analysis and quantification of the diversities of aerosol life cycles within
830 AeroCom, *Atmospheric Chemistry and Physics*, 6, 1777-1813, 2006.

831 Tilmes, S., Lamarque, J.-F., Emmons, L., Kinnison, D., Ma, P.-L., Liu, X., Ghan, S., Bardeen,
832 C., Arnold, S., and Deeter, M.: Description and evaluation of tropospheric chemistry and
833 aerosols in the Community Earth System Model (CESM1. 2), *Geoscientific Model*
834 *Development*, 8, 1395-1426, doi:10.5194/gmd-8-1395-2015, 2015.

835 Tomasi, C., Caroli, E., and Vitale, V.: Study of the Relationship between Ångström's
836 Wavelength Exponent and Junge Particle Size Distribution Exponent, *Journal of Climate and*
837 *Applied Meteorology*, 22, 1707-1716, 10.1175/1520-
838 0450(1983)022<1707:SOTRBW>2.0.CO;2, 1983.

839 US-EPA: 2005 National Emissions Inventory (NEI), US Environmental Protection Agency in,
840 available at: ftp://aftp.fsl.noaa.gov/divisions/taq/emissions_data_2005/, 2009.

841 Vinken, G. C. M., Boersma, K. F., van Donkelaar, A., and Zhang, L.: Constraints on ship NO_x
842 emissions in Europe using GEOS-Chem and OMI satellite NO₂ observations, *Atmospheric*
843 *Chemistry and Physics*, 14, 1353-1369, 10.5194/acp-14-1353-2014, 2014.

844 von Engel, A., and Teixeira, J.: A Planetary Boundary Layer Height Climatology Derived
845 from ECMWF Reanalysis Data, *Journal of Climate*, 26, 6575–6590, doi: 10.1175/JCLI-D-12-
846 00385.1, 2013.

847 Weigum, N., Schutgens, N., and Stier, P.: Effect of aerosol subgrid variability on aerosol
848 optical depth and cloud condensation nuclei: implications for global aerosol modelling,
849 *Atmospheric Chemistry and Physics*, 16, 13619-13639, 10.5194/acp-16-13619-2016, 2016.

850 Whitburn, S., Van Damme, M., Clarisse, L., Bauduin, S., Heald, C., Hadji-Lazaro, J.,
851 Hurtmans, D., Zondlo, M. A., Clerbaux, C., and Coheur, P.-F.: A flexible and robust neural
852 network IASI-NH₃ retrieval algorithm, *J. Geophys. Res.-Atmos.*, In Press,
853 10.1002/2016JD024828, 2016.

854 Wild, O., Zhu, X., and Prather, M. J.: Fast-J: Accurate Simulation of In- and Below-Cloud
855 Photolysis in Tropospheric Chemical Models, *Journal of Atmospheric Chemistry*, 37, 245-282,
856 10.1023/a:1006415919030, 2000.

857 Zhang, X., Chen, Z. M., Wang, H. L., He, S. Z., and Huang, D. M.: An important pathway for
858 ozonolysis of alpha-pinene and beta-pinene in aqueous phase and its atmospheric implications,
859 *Atmospheric Environment*, 43, 4465-4471, 10.1016/j.atmosenv.2009.06.028, 2009.

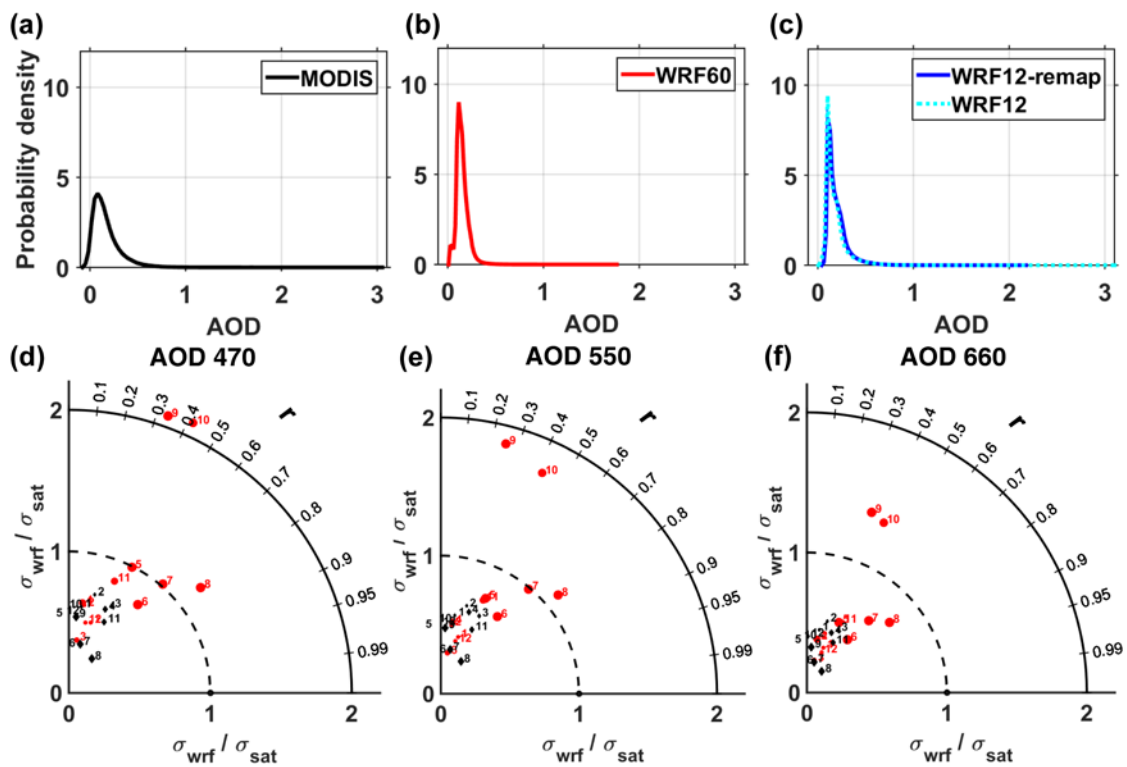
860 Zhang, Y., He, J., Zhu, S., and Gantt, B.: Sensitivity of simulated chemical concentrations and
861 aerosol-meteorology interactions to aerosol treatments and biogenic organic emissions in
862 WRF/Chem, *Journal of Geophysical Research: Atmospheres*, 121, 6014-6048,
863 10.1002/2016JD024882, 2016.

864 Zieger, P., Fierz-Schmidhauser, R., Weingartner, E., and Baltensperger, U.: Effects of relative
865 humidity on aerosol light scattering: results from different European sites, *Atmospheric*
866 *Chemistry and Physics*, 13, 10609-10631, 10.5194/acp-13-10609-2013, 2013.

867

868

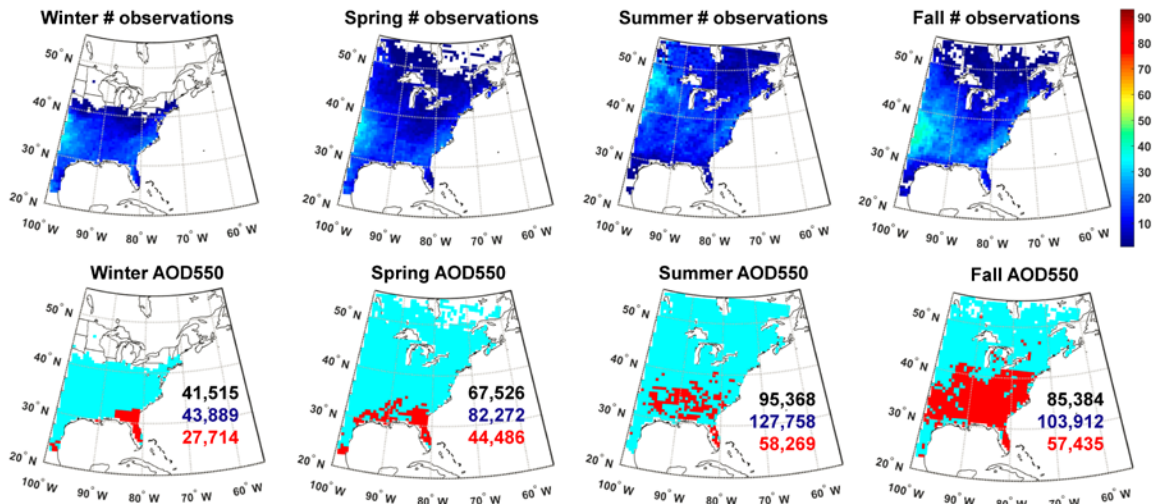
870



871

872 **Figure 1. Probability density function of once daily AOD at a wavelength (λ) of 550 nm**
 873 **for (a) MODIS, (b) WRF60 and (c) WRF12 and WRF12-remap during the year 2008. (d-**
 874 **f) Taylor diagrams of mean monthly AOD at wavelengths (λ) of (d) 470, (e) 550 and (f)**
 875 **660 nm as simulated by WRF-Chem at different resolutions (black diamonds=WRF60**
 876 **and red dots=WRF12-remap) relative to MODIS observations. The numbers by each**
 877 **symbol denote the calendar month (e.g. 1=January).**

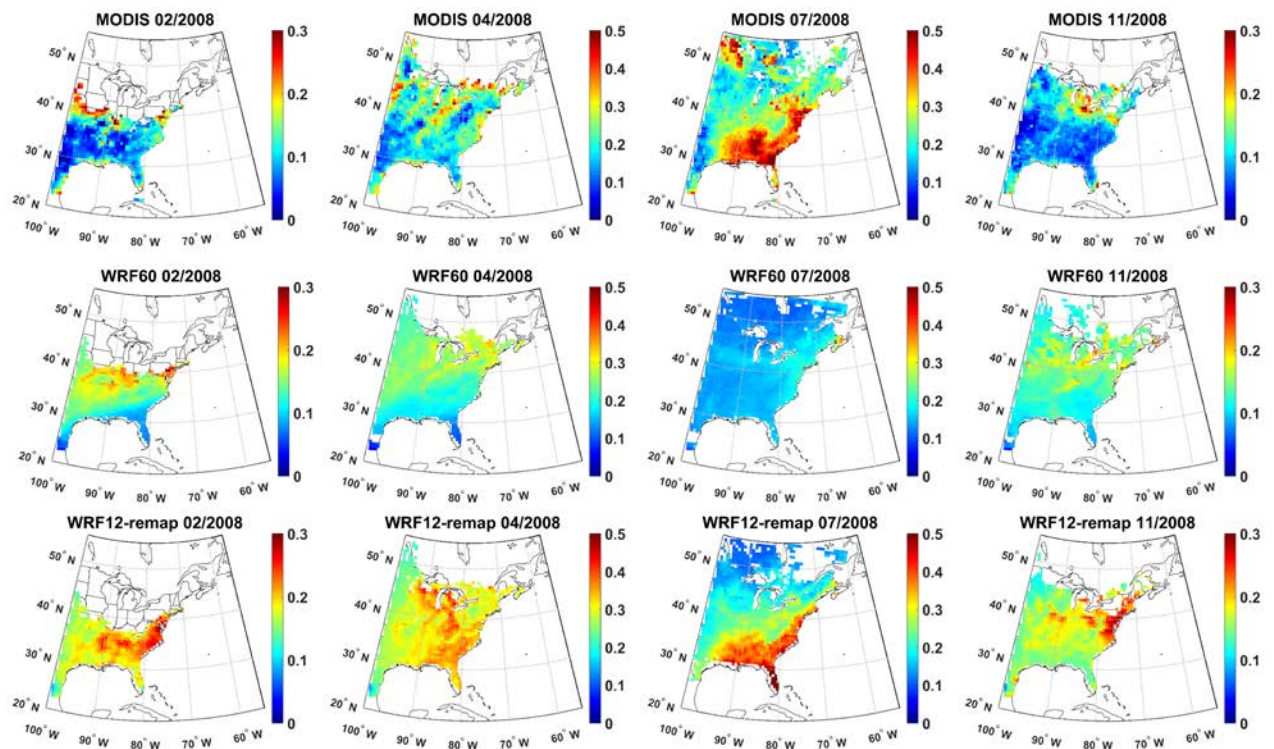
878



879

880 **Figure 2. First line: Number of paired AOD observations at a wavelength (λ) of 550 nm**
 881 **(i.e. simultaneous values as output from WRF-Chem and observed by MODIS) used to**
 882 **perform a t-test designed to evaluate whether the difference computed for each grid cell**
 883 **as WRF60-MODIS differs from that computed as WRF12-remap-MODIS on a seasonal**
 884 **basis (columns show Winter (DJF), Spring (MAM), Summer (JJA) and Fall (SON)).**
 885 **Second line: Results of the t-test. Pixels that have p-values that are significantly different**
 886 **at $\alpha=0.10$ are indicated in red and have been corrected for multiple testing using a False**
 887 **Discovery Rate approach. The number of observations of cloud-free conditions summed**
 888 **across all days in each season and all grid cells is also reported (black=MODIS,**
 889 **blue=WRF60, red=WRF12-remap).**

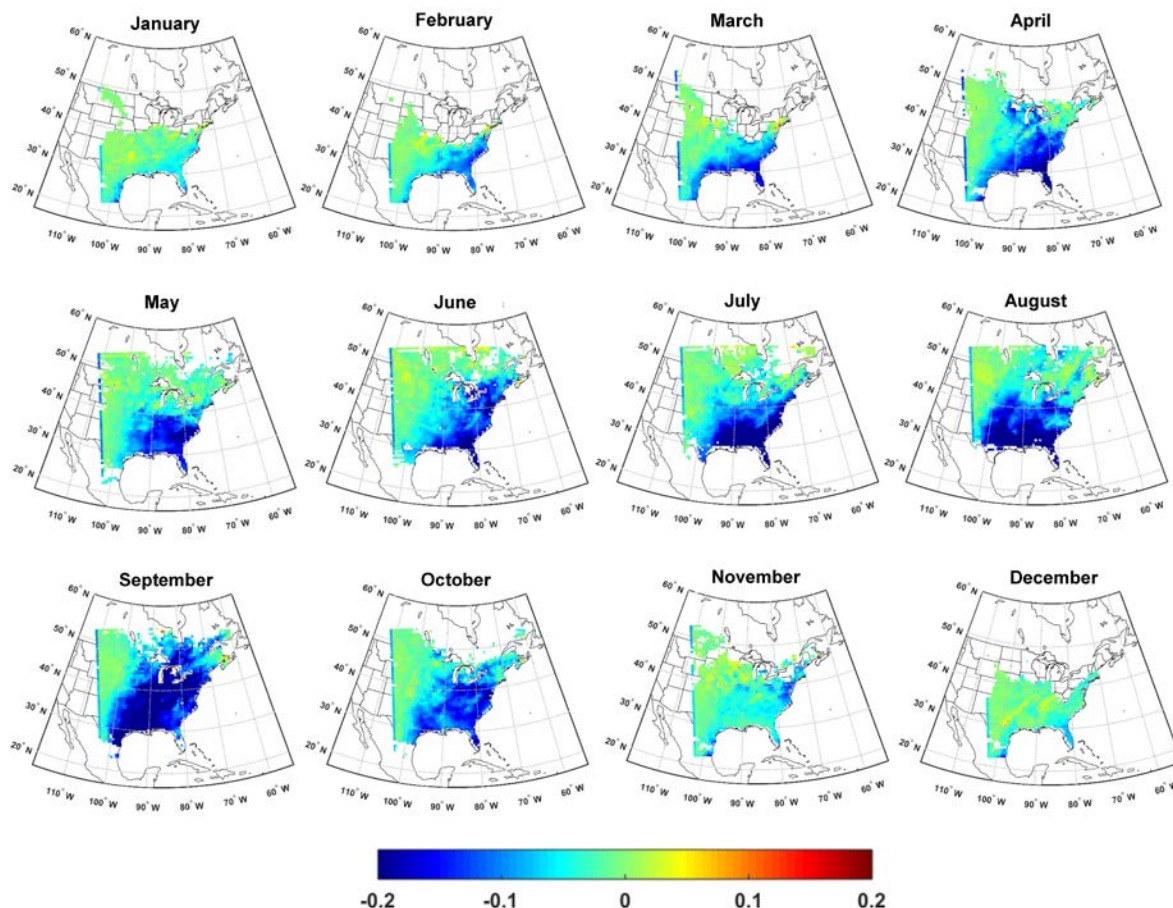
890



891

892 **Figure 3. Monthly mean AOD at a wavelength (λ) of 550 nm from MODIS (first line) and**
 893 **WRF-Chem at different resolutions (WRF60 and WRF12-remap, second and third line)**
 894 **during a representative month in each climatological season (columns). Note that a**
 895 **different color scale is applied for different months. For a monthly mean value for a grid**
 896 **cell to be shown, there must be at least 5-simultaneous daily values (for the time of the**
 897 **satellite overpass) available.**

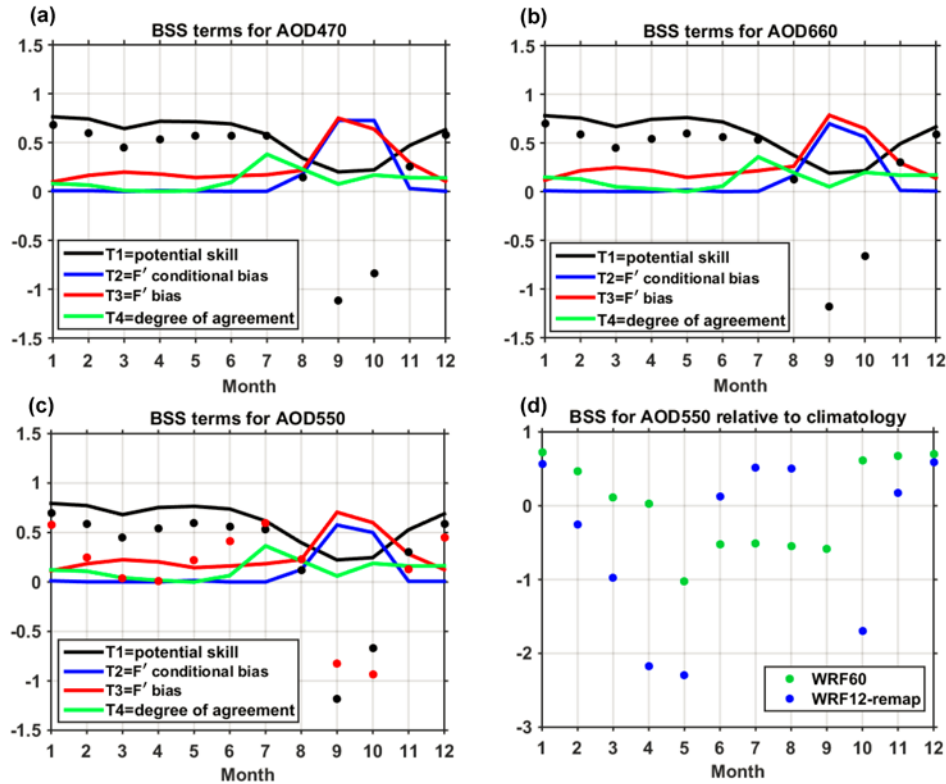
898



899

900 **Figure 4.** Difference in monthly mean AOD at a wavelength (λ) of 550 nm between WRF-
 901 Chem simulations conducted at 60 km resolution (WRF60) and output from WRF-Chem
 902 simulations conducted with a resolution of 12 km but remapped to 60 km (WRF12-
 903 remap). Differences are computed as WRF60 minus WRF12-remap. Similar spatial
 904 patterns and magnitudes of differences are found for λ of 470 and 660 nm. The calendar
 905 months of 2008 are shown in the titles of each panel.

906

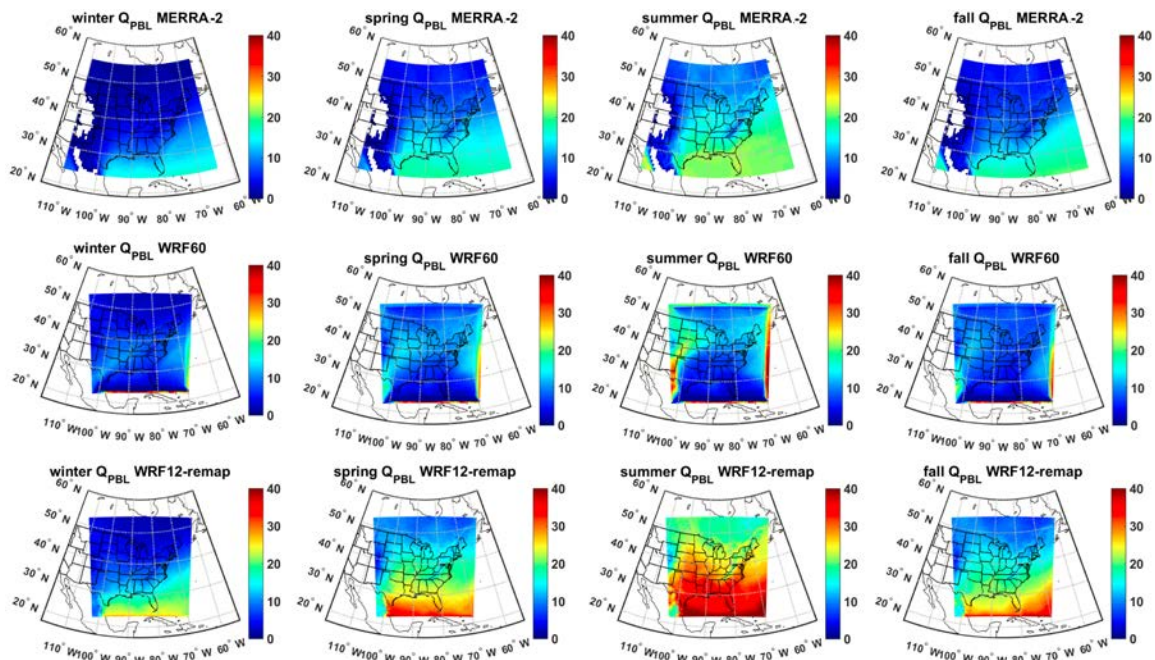


907

908 **Figure 5. (a-c) Brier Skill Scores (BSS, black dots) for monthly mean AOD by calendar**
 909 **month (1=January) for AOD at 470, 550 and 660 nm. In this analysis of model skill**
 910 **WRF12 output is mapped to the WRF60 grid (WRF12-remap) and BSS are computed**
 911 **using MODIS as the target, WRF60 (driven by NAM12 meteorological boundary**
 912 **conditions) as the reference forecast and WRF12-remap as the forecast. Also shown by**
 913 **the color lines are the contributions of different terms to BSS. In panel c the red dots**
 914 **indicate BSS when the reference forecast is WRF60 driven by GFS meteorological**
 915 **boundary conditions. (d) BSS of monthly mean AOD from WRF60 (green dots) and**
 916 **WRF12-remap (blue dots) relative to MODIS monthly mean climatology during 2000-**
 917 **2014 (reference forecast). Monthly mean AOD from MODIS are used as the target. BSS**
 918 **for WRF12-remap in September is -6.1.**

919

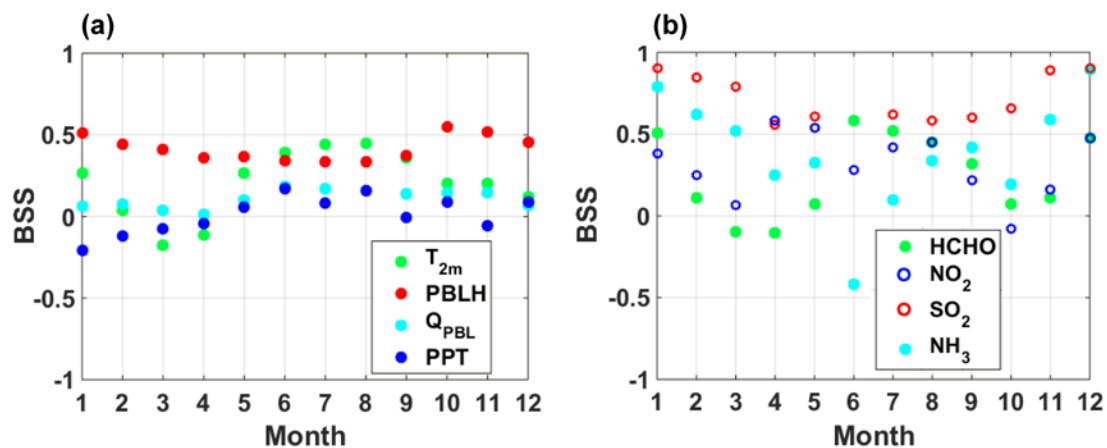
920



921

922 **Figure 6. Seasonal mean specific humidity [kg m^{-2}] integrated from the surface to 825 hPa**
 923 **(Q_{PBL}) from MERRA-2 (first row) assuming an average air density in the PBL of 1.1 kg**
 924 **m^{-3} , WRF60 (second row), and WRF12-remap (third row). The data are 3-hourly and**
 925 **show only cloud-free hours in all three data sets.**

926



927

928 **Figure 7. Brier Skill Scores (BSS) for key (a) meteorological and (b) chemical variables.**

929 **BSS are computed using hourly data of T at 2m (T_{2m}) and PBLH, 3-hourly estimates of**

930 **specific humidity in the boundary layer (Q_{PBL}), and z-scores of monthly total precipitation**

931 **(PPT), and of monthly mean columnar gas phase concentrations.**

932

933

934 **Tables**

935 **Table 1. Physical and chemical schemes adopted in the WRF-Chem simulations presented**
 936 **herein.**

Simulation settings	Values
Domain size	300 × 300 (60 × 60) grid points
Horizontal resolution	12 km (60 km)
Vertical resolution	32 levels up to 50 hPa
Timestep for physics	72 s (300 s)
Timestep for chemistry	5 s
Physics option	Adopted scheme
Microphysics	WRF Single-Moment 5-class (Hong et al., 2004)
Longwave Radiation	Rapid Radiative Transfer Model (RRTM) (Mlawer et al., 1997)
Shortwave Radiation	Goddard (Fast et al., 2006)
Surface layer	Monin Obhukov similarity (Janjić, 2002; Janjić, 1994)
Land Surface	Noah Land Surface Model (Chen and Dudhia, 2001)
Planetary boundary layer	Mellor-Yamada-Janjich (Janjić, 1994)
Cumulus parameterizations	Grell 3D (Grell and Dévényi, 2002)
Chemistry option	Adopted scheme
Photolysis	Fast J (Wild et al., 2000)
Gas-phase chemistry	RADM2 (Stockwell et al., 1990)
Aerosols	MADE/SORGAM (Ackermann et al., 1998; Schell et al., 2001)
Anthropogenic emissions	NEI (2005) (US-EPA, 2009)
Biogenic emissions	Guenther, from USGS land use classification (Guenther et al., 1994; Guenther et al., 1993; Simpson et al., 1995)

937

938

939 **Table 2. Spearman correlation coefficients (ρ) between AOD at wavelengths (λ) of 470,**
940 **550 and 660 nm from MODIS observations averaged over 12 or 60 km and WRF-Chem**
941 **simulations conducted at 60 km (WRF60, shown in the table as -60), at 12 km (WRF12,**
942 **shown in the table as -12), and from WRF-Chem simulations at 12 km but remapped to**
943 **60 km (WRF12-remap, shown in the table as -remap). Given WRF12-remap is obtained**
944 **by averaging WRF12 when at least half of the 5×5 12 km resolution cells contain valid**
945 **data, ρ from WRF60 and WRF12-remap may be computed on slightly different**
946 **observations and sample size. The bold text denotes correlation coefficients that are**
947 **significant at $\alpha=0.05$ after a Bonferroni correction is applied (i.e. $p \leq \frac{0.05}{9 \times 12} = 4.63 \times 10^{-4}$**
948 **is significant). The yellow shading is a visual guide that shows for each month and λ the**
949 **model output that has highest ρ with MODIS.**

Month→/ Variable↓	Jan	Feb	Mar	Apr	May	Jun	Jul	Aug	Sep	Oct	Nov	Dec
470-12	0.238	0.150	0.137	0.147	0.377	0.581	0.610	0.723	0.352	0.306	0.259	0.212
470-60	0.156	0.226	0.438	0.412	-0.219	-0.146	0.379	0.601	0.087	-0.051	0.500	-0.059
470-remap	0.295	0.197	0.250	0.182	0.516	0.637	0.675	0.777	0.368	0.441	0.315	0.274
550-12	0.223	0.124	0.142	0.146	0.349	0.541	0.580	0.689	0.275	0.301	0.280	0.215
550-60	0.179	0.244	0.429	0.332	-0.288	-0.188	0.324	0.567	0.073	-0.077	0.491	0.002
550-remap	0.297	0.164	0.261	0.199	0.493	0.605	0.651	0.747	0.286	0.437	0.352	0.309
660-12	0.217	0.136	0.165	0.152	0.324	0.476	0.540	0.644	0.183	0.290	0.292	0.221
660-60	0.191	0.230	0.437	0.402	-0.305	-0.189	0.389	0.616	0.099	-0.137	0.536	0.049
660-remap	0.356	0.211	0.289	0.208	0.480	0.624	0.669	0.772	0.371	0.432	0.393	0.368

950
951

952 **Table 3. Spatial coherence in the identification of extreme AOD values (i.e. areas with**
953 **AOD>75th percentile over space for each month) between WRF-Chem at different**
954 **resolutions relative to MODIS. No significant wavelength dependence is found for model**
955 **skill in identifying extreme AOD so results are only shown for $\lambda = 550$ nm. The different**
956 **model output is denoted by -60 for simulations at 60 km, -12 for simulations at 12 km**
957 **resolution, and as -remap for simulations at 12 km but with the output remapped to 60**
958 **km. The Accuracy (Acc) indicates the fraction of grid cells co-identified as extremes and**
959 **non-extremes between WRF-Chem and MODIS relative to the total number of cells with**
960 **valid data. The Hit Rate (HR) is the probability of correct forecast and is the proportion**
961 **of cells correctly identified as extremes by both WRF-Chem and MODIS. The yellow**
962 **shading indicates the model resolution with highest skill in each month for AOD at 550**
963 **nm.**

Month→/ Metric↓	Jan	Feb	Mar	Apr	May	Jun	Jul	Aug	Sep	Oct	Nov	Dec
Acc-12	0.673	0.665	0.659	0.638	0.710	0.800	0.855	0.839	0.666	0.679	0.723	0.661
Acc-60	0.707	0.778	0.735	0.730	0.600	0.587	0.658	0.769	0.661	0.637	0.729	0.681
Acc-remap	0.674	0.680	0.694	0.640	0.766	0.824	0.887	0.837	0.667	0.699	0.767	0.641
HR-12	0.346	0.331	0.319	0.275	0.421	0.599	0.711	0.678	0.333	0.358	0.447	0.323
HR-60	0.417	0.558	0.471	0.460	0.200	0.173	0.315	0.538	0.321	0.274	0.458	0.364
HR-remap	0.350	0.361	0.387	0.281	0.532	0.649	0.775	0.674	0.333	0.399	0.535	0.284

964
965
966
967
968
969
970
971